Air quality in the middle and lower reaches of the Yangtze River channel: A cruise campaign

Zhong Li[1], Chunlin Li[1,2], Xingnan Ye[1], Hongbo Fu[1], Lin Wang[1], Xin Yang[1], Xinke Wang[3], Zhuohui Zhao[4], Haidong Kan[4], Abdelwahid Mellouki[5], Jianmin Chen[1,4,*]

[1] *Shanghai Key Laboratory of Atmospheric Particle Pollution and Prevention, Fudan Tyndall Center, Department of Environmental Science & Engineering, Institute of Atmospheric Sciences, Fudan University, Shanghai 200433, China*

[2] *Department of Earth and Planetary Sciences,Weizmann Institute of Science*

[3] *Univ Lyon, Université Claude Bernard Lyon 1 CNRS, IRCELYON, F-69626, Villeurbanne, France*

[4] *School of Public Health, Fudan University, Shanghai 200032, China*

[5] *Institut de Combustion, Aérothermique, Réactivité et Environnement, CNRS, 45071 Orléans cedex 02, France*

[*] **Correspondence to:** Jianmin Chen (jmchen@fudan.edu.cn)

Abstract

Yangtze River is the longest river in China, nearly one-third of the national population lives along the river. Air quality over the Yangtze River is interesting as it may have significant influences on the aquatic ecosystem, health of everyone living along the Yangtze River, and regional climate change. Chemical compositions of ambient aerosol were determined during a comprehensive cruise campaign carried out along the Mid-Lower Reaches Yangtze River (MLYR) in winter of 2015. The total average concentration of $PM_{2.5}$ were 119.29 ± 33.67 μg m^{-3}, and the dominate ionic composition in $PM_{2.5}$ was were SO_4^{2-} with an average concentration of 15.21 ± 6.69 μg m^{-3}, followed by NO_3^- (13.76 ± 4.99μg m^{-3}), NH_4^+ (9.38 ± 4.35μg m^{-3}) and Ca^{2+}(2.23 ± 1.24μg m^{-3}) in this cruise. Based on the filter samples, the concentration and chemical composition of $PM_{2.5}$ were remarkably varied or fluctuated from coastal areas to inland over the MLYR region. Crustal elements (Ca, Mg, Al and K) from floating dust showed peak concentrations in the Yangtze River Delta (YRD) region, while secondary inorganic species (SO_4^{2-}, NO_3^- and NH_4^+) and some most enriched elements (Pb, As, Se and Cd) presented the high levels in central China (Wuhan region). The significant correlation between Se and SO_4^{2-} suggested that coal combustion may play an important role in secondary inorganic aerosol formation. The relative high enrichment factors (EFs) of Ca (EFs > 100) suggested the crustal elements may derive from anthropogenic sources. Furthermore, the concentration of levoglucosan in $PM_{2.5}$ and CO column level from satellite observation greatly enhanced in the rural areas (Anhui and Jiangxi), indicating that biomass burning may make remarkable contribution to the rural area. The concentrations of typical tracer for heavy oil (V and Ni) significantly increased in the Shanghai port, that was mainly ascribed to the ship emission, based on the air mass source analysis and the relatively high ratio of V/Ni as well. The results shown herein portrayed a good picture of air pollution along the Yangtze River.

Keywords:

Shipboard observation, chemical composition, ship emission, Yangtze River

1 Introduction

Yangtze River is the longest river in China, originating from the Qinghai-Tibetan Plateau and extending to the East China Sea, and it drains an area of 18,08,500 square km basin, of which is China's great granary, and feeds nearly one-third of the national population (Liu et al., 2007; Jiang et al., 2008). Currently, three densely city agglomerations, including Wuhan, Nanjing, and Shanghai (WNS), which

are the centers of economy, transportation, politics, and culture in central and eastern China, and all of which are home to larger petrochemical complex and/or steel industry, have formed along both shores of the Mid-Lower Reaches Yangtze River (MLYR). The MLYR region is one of the most developed and economically vibrant regions in China, accounting for 34.13% of China's total GDP in 2015. Owing to fast economic development and industrialization, this region has become one of the most polluted areas in China (Xu et al., 2016b).

Fine aerosol particles are becoming more important in recent years, due to their negative effects on human health, agriculture, and climate change (Wang et al., 2012; Kang et al., 2013b; Pöschl, 2005; Seaton et al., 1995; Ackerman et al., 2004; Stier et al., 2005; Chameides et al., 1999; Novakov and Penner, 1993; Jones et al., 1994). Numerous field observations related to fine particles have been conducted in the megacities in the Yangtze River Delta (YRD) region, especially in Nanjing and Shanghai. Over the past years, the variation of mass concentrations, chemical compositions, size distributions, seasonal variations, daily change, optical properties, and temporal-spatial distributions of fine particles in this region have been investigated, and the causes and impacts of aerosol pollution have also been generally studied (Zhou et al., 2016; Kang et al., 2013b; Tao et al., 2014b; Shen et al., 2014; Fu et al., 2014; Huang et al., 2013; Huang et al., 2012b; Huang et al., 2012a; Ding et al., 2013a; Ding et al., 2017; Zhang et al., 2010). By analysis of several serious haze cases, Huang et al. (2012) pointed out that secondary inorganic and dust episodes always erupted in spring, while biomass burning (BB) event was often observed in summer (harvest season for wheat). Further, the high sulfate oxidizing rate (SOR) and nitrate oxidizing rate (NOR) were also observed from long-term field measurements in Nanjing and Shanghai, indicating that photochemical reactions in the atmosphere were quite active in these areas (Zhou et al., 2016; Zhou et al., 2017; An et al., 2015). Wang et al. (2015b) also found that secondary pollutants contributed the major fraction of aerosol mass, especially in Shanghai-Nanjing city cluster. The increasing trend of the NO_3^-/SO_4^{2-} rations since the year 2000 suggested that vehicle sources became more important in this region (Kang et al., 2013a; Huang et al., 2012a; Tao et al., 2014b; Sun et al., 2017). Beyond, Cheng et al. (2014) estimated that BB contributed 37% of $PM_{2.5}$, 70% of organic carbon, and 61% of element carbon in harvest, respectively. If BB was controlled and even forbidden in this season, the $PM_{2.5}$ levels would decrease by 47% in the YRD region (Cheng et al., 2014). Some typical events, including fresh combustion pollution from firework (Zhang et al., 2010; Kong et al., 2015), and the peak of secondary inorganic aerosol species (SNA, SO_4^{2-}, NO_3^-, and NH_4^+) deriving from the travel rush and re-opening of

factories after China Spring Festival (Huang et al., 2012b; Kong et al., 2015), have also been focused and analyzed. Huang et al. (2013) also investigated the chemical composition of fine particles in Shanghai, finding that the concentrations of anthropogenic calcium drastically decreased as results of strict monitoring and implementing control of construction activity during 2010 Word Expo. Compared with normal (pre-control) periods, the levels of Ca^{2+} and SO_2 also reduced 55% and 46% during the 2014 Youth Olympic Games, respectively (Zhou et al., 2017).

The MLYR region faces the most complex anthropogenic emission sources, including a variety of power plants, large petrochemical and steel industries, and farmland distributed along both banks of the Yangtze River, as well as ship emissions. It was well documented that ship emissions displayed a significant impact on regional air quality, particularly in traffic hubs and harbors (Pandis et al., 1999; Becagli et al., 2017; et al., 2014). The contribution and effect of ship emissions to local air pollution, especially PM, have been briefly analyzed at levels from regional to global (Jalkanen et al., 2015; Zhan et al., 2014; Pandis et al., 1999; Fan et al., 2016; Coggon et al., 2012). The emission factors, and properties of emitted particles and gases from ship-plume in different engine speeds were also reported (Zhang et al., 2016; Moldanová et al., 2009; Agrawal et al., 2009). Ship-related pollutants have been identified in the YRD port cluster and surrounding area. In 2010, SO_2, NO_x, and $PM_{2.5}$ from ship emissions in the YRD port cluster were up to 3.8×10^5 t/y, 7.1×10^5 t/y, and 5.1 × t/y, respectively. The maximum SO_2 and NOx concentrations from ship emissions in harbors or traffic hubs were nearly 36 times and 17 times higher than the maximum land-based emissions, respectively (Fan et al., 2016). Zhao et al. (2013b) pointed out that Ni and V enriched in submicron particles in Shanghai port. Recently, Liu et al. (2017) also reported that ship-plume contributed to 2-7 μg m^{-3} to fine particle within the coastal of Shanghai port, accounting for 20-30% of total $PM_{2.5}$. Known as “golden canal”, Yangtze River was an important route for trade and travel. However, there is seldom data related to air quality and the influence of ship emissions along the Yangtze River channel. Meanwhile, related observations with the synchronous trend of aerosol in the MLYR region remain insufficient.

To characterize air quality in this region, a round-trip field observation voyage, namely Yangtze River Campaign (YRC), was carried out between Shanghai and Wuhan. This cruise aimed to characterize the chemical components of atmospheric pollutants, to analyze these spatial distributions, and to identify potential source contribution. To the best of our knowledge, it is the first systematic observation on air pollution along the largest and longest river in China.

2 Measurements and methods

2.1 Overview YRC

A mobile monitoring platform (A container: length 10.0 m, width 4.0 m, and height 2.5m) was placed on a vessel (length: 20 m, width 6 m), sailing from 22 November to 05 December in 2015 along the Yangtze River channel between Shanghai to Wuhan (29.72˚N-32.33˚N, 114.33˚E-121.61˚E). This campaign route is illustrated in Figure 1. Starting on 22 November in the Waigaoqiao port of Shanghai, then the vessel crossed Jiangsu, Anhui province, and finally arrived at the Hankou port in Wuhan, Hubei province on 29 November along the Yangtze River waterway. The ship shifted at an average speed of 1 m/s heading the upper the Yangtze River towards Wuhan. After berthing in the port of Wuhan one night, the vessel turned around, departed, and shifted towards Shanghai. This cruise finally ended in the Waigaoqiao port in Shanghai on 5 December. During YRC, a wide range of data, including common meteorological parameters, trace gas concentrations (CO, NO-NO_x, SO_2, and O_3), chemical composition of aerosol particles, and satellite dataset over this region were acquired and analyzed.

2.2 Trace gases measurements

A serious of commercial trace gas instruments, including 43i SO_2 analyzer, 48i CO analyzer, and 42i NO-NO_2-NO_x analyzer (Thermo Environmental Instruments Ins., USA C-series), were installed in an air-conditioned container to measure the concentration of gaseous pollutants. The routine procedures of QA/QC (the daily zero/standard calibration) were performed, according to the technical guidance by U.S. Environmental Protection Agency (USEPA, 1998).

Trace alkanes, including toluene and benzene, were also sampled in stainless summa canister, and quantified by a gas chromatograph with a mass spectrometer and a flame ionization detector (GC-MS/FID) (Wang et al., 2014). The sampling interval of VOCs was 3 hours with fluctuation. The ratio of toluene/benzene (T/B) was commonly regarded as an indicator of the photochemical processing (Baltrenas et al., 2011). The high ratio of T/B indicated that air masses were fresh emissions, while lower value suggested that air masses had undergone photochemical processes. In this paper, we used the same value ratio of T/B in CalNex (Gaston et al., 2013). Air masses with T/B << 1 were excepted to well undergo photochemical aging while urban fresh air masses had much higher T/B ratio ($\geqslant$2). Ship track self-emission was removed by subducting the periods when the winds blew from the stern, that is, the

relative wind direction was from 130˚ to 220˚ to the ship direction (0˚ in the front). The real-time measurement of trace gases and aerosol data presented here were filtered out by this method.

2.3 Chemical analysis of the filter samples

Particulate samples of $PM_{2.5}$ and $PM_{1.0}$ were simultaneously collected on separate quartz filters (*Φ*90 mm, Whatman Inc., Maidstone, UK) using a medium-volume sampler by HY-100 (Qingdao Hengyuan S.T. Development Co., Ltd, China) (model: $PM_{2.5}/PM_{1.0}$; flow rate: 100 L min^{-1}, respectively), which was placed on the foredeck at approximately 3.0 m above sea level. The duration time of collecting sample was generally set at 12 h (in parallels: day 07:00-19:00, night 19:00-07:00), while it was also collected PM for 24 h. High-purity quartz filters were preheated at 500 ℃ for 10 h to virtually eliminate the residues prior to sampling. All the samples were stored in a refrigerator keeping at -20 ℃ for analysis. The filter sample masses were measured by an intelligent weight system (Hangzhou Wmade Intelligent Technology co., LTD) which was maintained in constant condition (Temperature (T): 20 ℃ and Relative humidity (RH): 40%). All the procedures were well documented, and supervised to avoid the possible contaminations. The sample instruments were placed on the bow of the ship far away from its track. Ship self-emission in the filter samples was ignored, since the most prevailing winds blew from the bow to the stern during the sampling periods.

One-eighth of each filter was extracted ultrasonically by 20 mL of deionized water (18.2 MΩ cm^{-1}) for 40 min. After filtering, eight inorganic ions (SO_4^{2-}, NO_3^-, Cl^-, NH_4^+, Na^+, K^+, Ca^{2+}, and Mg^{2+}) were analyzed by an ion chromatography (940 Professional IC, Metrohm, Switzerland), and a sugar column coupled with pulsed electrochemical detection (945 Professional Detector Vario, Metrohm, Switzerland) was used to measure levoglucosan (lev) in the extract. Both of instruments were controlled with a IC software. The lower and upper limits of the detection were 0.5 and 4 μg m^{-3}, respectively. The relative standard deviation of each ion was less than or equal to 2% from three reproducibility tests. Blank samples were analyzed with the same processes to remove potentially contaminations.

One-eighth of the sample filter and the blank filter were cut into fragments, and digested at 170 ℃ for 4 h in a high-pressure Teflon digestion vessel with 3 mL of HNO_3 and 1 mL of $HClO_4$ (Wang et al., 2006; Li et al., 2015b). After cooling, the digested solution was filtered and diluted to 15 mL with ultrapure Mill-Q water. An inductively coupled plasma mass spectrometer (ICP-MS, Agilent 7500a) was employed to measure the concentrations of 17 elements (Al, As, Ca, Co, Cr, Cu, Fe, K, Mg, Mn, Na, Ni,

Se, Tl, Pb, V, and Zn) in the filter samples. National standard material (soil, GSS-12, China) was also digested, and used to calculate the element recoveries ranging from 91%-102%. The detection limits of the trace elements were derived from the standard deviation (3δ) of the blank values. Details relating to ICP-MS have been described in elsewhere (Li et al., 2015b).

Organic carbon (OC) and elemental carbon (EC) in the aerosol samples were analyzed by a Thermal/Optical Carbon Analyzer (DRI Model 2001). Each sample was identified as four OC fractions (OC1, OC2, OC3, and OC4 at 120, 250, 450, and 550 ℃, respectively, in a helium-air) and three EC fractions (EC1, EC2, and EC3 at 550,700, and 800 ℃, respectively, in the mixture air (98% helium and 2% oxygen) by an IMPROVE thermal/optical reflectance (TOR) protocol. Pyrolyzed organic carbon (POC) was separately detected by transmittance. IMPROVE OC was defined as OC1 + OC2 + OC3 + OC4 + POC, and EC was calculated by EC1 + EC2 + EC3 − POC.

2.4 Satellite data and ship traffic data

The satellite databases, including Moderate Resolution Imaging Spectroradiometer (MODIS) with a resolution of 10 × 10 km, Measurement of Pollutants in the Troposphere (MOPITT) and Ozone Monitoring Instrument (OMI) on the National Aeronautics reaching a spatial resolution of 13 × 24 km at nadir, and Space Administration's Earth Observing System (NASA's EOS) Aura satellite, were applied to provide spatial distribution of aerosol particles and trace gases (Xu et al., 2011; Huang et al., 2012a). The column levels of CO, NO_2, SO_2, and aerosol optical depth (AOD) were retrieved over the MLYR region. In this study, all of data from satellite datasets were interpolated and averaged into grid cells with a 0.25° × 0.25° resolution.

Ship positions and numbers in the Yangtze River channel were decoded by Automatic Identification System (AIS) databases which were obtained from the Marine Department. A 15-day AIS datasets along the Yangtze River were selected with a high time resolution (about 15min).

2.5 Potential source contribution function

The potential source contribution function developed by Hopke et al. (1995) was applied to derive the potential source regions and spatial distributions. In this study, 3 day back trajectories arriving at height of 500 m was calculated using National Oceanic and Atmospheric Administration's (NOAA's) Hybrid Single Particle Lagrangian Integrated Trajectory (HYSPLIT-4) model (http://www.arl.noaa.gov/ready/open/hysplit4.html) with global meteorological data from NCEP reanalysis data (ftp://arlftp.arlhq.noaa.

gov/pub/archives/rean-alysis) (Draxler and Hess, 1998). The contribution of the potential sources during YRC was calculated by the PSCF analysis with TrajStat (Wang et al., 2009). The domain sources were restricted to 25°N-45°N and 110°E-125°E, which were divided into grid cells with a 0.5°×0.5° resolution.

The PSCF value for the *ij* th grid cell was defined as:

$$\mathrm{PSCF}_{ij} = \frac{\mathrm{M}_{ij}}{\mathrm{N}_{ij}} W_{ij} \quad (1)$$

where N_{ij} is the total number of trajectory segment endpoints that fall in the *ij* cell, and M_{ij} is the number of endpoints for the same cell with arrival times at the sampling site, corresponding to pollutant concentrations higher than an arbitrary criterion value. In this study, the average concentration for each trace element was set as the criteria value. To reduce the random error and uncertainty of the small value of n_{ij}, the weighting function of W_{ij} reduced the PSCF values when the total number of the endpoints in a particular cell n_{ij} was less by approximately 3 times than the average $\mathrm{N}_{\mathrm{Ave}}$ value of the endpoints per each cell (Han et al., 2005):

$$\mathrm{W}_{ij} = \begin{cases} 1.00 & \mathrm{N}_{ij} > 3\mathrm{N}_{\mathrm{Ave}} \\ 0.70 & 1.5\mathrm{N}_{\mathrm{Ave}} < \mathrm{N}_{ij} \leq 3\mathrm{N}_{\mathrm{Ave}} \\ 0.42 & \mathrm{N}_{\mathrm{Ave}} < \mathrm{N}_{ij} \leq 1.5\mathrm{N}_{\mathrm{Ave}} \\ 0.17 & 0 < \mathrm{N}_{ij} \leq \mathrm{N}_{\mathrm{Ave}} \end{cases} \quad (2)$$

3 Results and discussion

3.1 Classification of the typical pollution episodes

The air pollution during the cruise was classified into eight distinct episodes, based on sampling locations, backward trajectories, and photochemical processes (T/B value) (Figure 1, Figure S1, Figure S2 and Table 1). The detailed meteorological information over the MLYR region was also summarized in the supporting information. As shown in Figure S1, the first episode (EP-1), starting from 22 to 23 November, was characterized by the sampled air masses which came from the East China Sea, and were typically influenced by the local industry and Shanghai harbor pollution. The ratio of T/B ranged from 0.6 to 2 with an average of 1.3, suggesting fresh air masses mixed by the aged ones. The air masses in the secondary episode (EP-2), with B/T<1, originated from the rural areas (Anhui and Henan), carrying agriculture emission (Figure S2). Sampled air masses stagnated around Jiujiang to Wuhan from the third episode (EP-3) to the fifth episode (EP-5). However, the fourth episode (EP-4) (Wuhan region) with the low average T/B ratio of 0.97 undergone well atmospheric aging. The local air during EP-4 was in low

pressure system with low wind speeds that didn't favor the diffusion of the local pollution (Figure S3). Air mass with T/B ratio $\geqslant$ 2 were identified from fresh emissions. Both EP-3 and EP-5 (nearly Jiujiang) were characterized by high T/B value (Figure S2), suggesting that these two pollution episodes were contributed mainly from regional fresh emissions. For the sixth episode (EP-6), the wind direction shifted from southwest to northwest, and the vessel was again traveling through the rural area of middle reach of Yangtze River, suggesting that air masses may originate from agricultural activities. Then in the seventh episode (EP-7), a cold front arrived, and wind speeds increased significantly from average 3.84 m/s to 5.38 m/s (Table 2) with air masses transported from northern inland regions, which was further confirmed by wind fields (Figure S3) and the sharply decreases of RH (Table 2). The last episode (EP-8) was in the YRD region where highly intensive anthropogenic activities released a large amount of the pollutants. Air masses in EP-8, with the average T/B value of 1.73, were expected to mixture of aged masses sources with regional fresh emissions. Overall, EP-1 and EP-8 (the YRD region) were mainly influenced by fresh local emissions mixed with aged air masses, while agriculture emissions contributed significantly during EP-2 and EP-6 episodes. Both EP-3 and EP-5 were characterized by fresh emissions, even though the megapolis was not available in this region. The cruise started on November 22, but the offline $PM_{2.5}$ samples were collected after November 25. Thus, EP-1 description was ignored in the present study.

3.2 Air pollution during YRC

3.2.1 Variability of air pollutants observed in the vessel

The $PM_{2.5}$ and $PM_{1.0}$ was sampled from 25 November to 5 December in 2015. The detail information is also summarized in Table 1. The average mass concentrations of $PM_{1.0}$ and $PM_{2.5}$ during YRC were 96.69 $\pm$ 22.18 $\mu g\ m^{-3}$ and 119.29 $\pm$ 33.67 $\mu g\ m^{-3}$, respectively. The average ratio of $PM_{1.0}/PM_{2.5}$ was 0.8 $\pm$ 0.085, implying that $PM_{2.5}$ mainly dominated by fine particles with the size of $<$ 1.0 μm. The detailed meteorological information, including T, RH, pressure, wind direction and wind speed, and trace gaseous in different episodes are also summarized in Table 2. The peak concentrations of $PM_{2.5}$ were observed in EP-4 and EP-7 (Table 1). However, there were obvious differences between EP-4 and EP-7 in the meteorological parameters and trace gases levels, indicating that these two pollution events were completely different. As mentioned in 3.1, sampled air masses in EP-4 mainly originated from local emissions, whereas EP-7 was influenced by a long-transport of air pollution.

As shown in Table 2, the average concentrations of CO, SO_2, and NO_X varied dramatically in the different pollution episodes. Average concentrations of CO, and SO_2 (993.96 ± 387.34, and 9.32 ± 4.33 ppbv, respectively) were slightly lower than those in the cities in winter, including Wuhan (1024.00, and 13.30 ppbv) (Wang et al., 2017), Nanjing (1096.00, and 13.09 ppbv) (Sun et al., 2017), Chengdu (1440.00, and 12.60 ppbv) (Liao et al., 2017), and Shanghai (1067.20, and 18.90 ppbv) (Huang et al., 2012a). CO level continued to rise since the start of the YRC, and finally peaked in EP-6 and EP-7. Meanwhile the SO_2 and NO_X levels were much lower in these two episodes, which were identified as the BB event. As previously reported, biomass burning could produce large amount of CO, while NO_X and SO_2 were not the major gaseous pollutants released from BB (Huang et al., 2012a; Ding et al., 2013b). The mean CO concentration in EP-7 reached to 1224.88 ppbv, which was close to the level recorded at Shanghai during the harvest season of wheat (June) (Huang et al., 2012a). The SO_2 concentrations in EP-3 and EP-8 greatly increased, which were close to the SO_2 level in the haze event in Shanghai (Huang et al., 2012a). This was partly caused by local fresh emissions (the high T/B in EP-3 and EP-8). Except for EP-6 and EP-7 (BB event), the NO_X concentration almost exceeded 50 ppbv along this cruise. The average mass concentration of NO_x in this cruise is 63.74 ± 41.08 ppbv, which was much higher than the mean level in Shanghai (42.40ppbv, 2012) (Han et al., 2015), and Guangzhou (39.14ppbv, 2012) (Zou et al., 2015) that represented typical urban NO_X level. The NO_X concentration peaked in EP-3, which was identified to mainly come from local emissions. The high NO_X level along YRC was identified to come from strong regional emission. It could be derived that multiple sources of air pollution distributed on both banks of the Yangtze River.

3.2.2 Regional distribution of air pollutants identified by remote sensing observation

The MLYR region is one of the most polluted areas in China, and the spatial distribution of various pollutants were apparently different from coastal to inland region. As shown in Figure 2a, the high average values of AOD retrieved from MODIS MOD04 were observed in eastern Jiangsu and Shanghai, etc, where human and industrial activities were concentrated, suggesting that anthropogenic emissions were dominated. However, there was much missing data of AOD in central China due to heavy clouds. As presented in Figure S4 of the MODIS true-color imagery on 28 November, thick clouds covered across central China. Besides, the average of AOD was about 0.45, which was slight lower than that in Shanghai in winter (0.55) (He et al., 2012), and background (0.65) in the North China plain (Xu et al., 2011). The AOD value in northern China was higher than that in southern China. As plotted in Figure

2b, CO surface mixing ratio calculated by MOPITT revealed that Shandong, Henan, and Anhui were exposed to elevated CO column concentrations. CO is an important tracer for the incomplete combustion sources, such as BB and fossil fuel combustions (Girach et al., 2014). BB should be major source for CO in the grain-producing areas (Huang et al., 2012; Ding et al., 2013).As mentioned in section 3.2.1, the peak CO level was also observed in Anhui and the west of Jiangsu, which was characterized by agriculture emissions (EP-6 and EP-7). However, the sources of CO in the northern China should further study in the future. The high levels of SO_2 was mainly observed in the east in Anhui and stretched to the Shanghai area (Figure 2c), suggesting high-sulfur fossil fuel were still widely utilized over the MLYP region. Whereas, SO_2 levels in Nanjing urban areas were measured at the background pollution levels. In general, NO_2 was regarded as a tracer for the local emission source, due to short lifetime in the atmosphere (Geng et al., 2009; Xu et al., 2011). NOx emissions mainly originated from vehicle and power plant (Fu et al., 2013). One can see that the NO_2 emission was characterized by strong local sources in north China and the YRD region (Figure 2d), which are in good agreement with the previous reports (Lin, 2011; Zhao et al., 2013a).

3.3 Chemical composition of fine particles during YRC and comparisons with other published data

The concentrations and mass fractions of the major ions and levoglucosan in $PM_{2.5}$ are shown in Figure 3. The water-soluble ions constitute one of the dominant components in atmospheric aerosol and determine the aerosol acidity (Kerminen et al., 2001), accounting for 37.43% and 40.15% in $PM_{2.5}$ and $PM_{1.0}$ during YRC, respectively. To access the data quality, ion balance gained by the major anions (SO_4^{2-}, NO_3^-, and Cl^-) and cations (Na^+, NH_4^+, K^+, Ca^{2+}, and Mg^{2+}) was calculated in this cruise. Both cations and anions are in the units of equivalent concentration (μ eq m^{-3}). There is a good correlation ($R^2 > 0.99$ and $R^2 > 0.98$, $P < 0.01$) between cation and anions (equivalent concentration) in $PM_{1.0}$ and $PM_{2.5}$, respectively, implying a high quality of data and same source of major ions in this cruise (Figure S5a) (Boreddy and Kawamura., 2015). Additionally, the relationship between NH_4^+ and Ca^{2+} *vs* SO_4^{2-} and NO_3^- was further investigated. As plotted in Figure S5b, the slopes of linear regression lines for [NH_4^++Ca^{2+}] *vs* [SO_4^{2-}+NO_3^-] in $PM_{2.5}$ and $PM_{1.0}$ were 1.171 and 1.154, respectively, suggesting that the alkaline substance in aerosol could completely neutralize SO_4^{2-} and NO_3^- during YRC.

For the ionic concentration, the most abundant species of $PM_{2.5}$ was SO_4^{2-} with a mean of 15.21 ± 6.69 μg m^{-3}, followed by NO_3^- (13.76 ± 4.99 μg m^{-3}), NH_4^+ (9.38 ± 4.35 μg m^{-3}), Ca^{2+} (2.23 ± 1.24 μg m^{-3}),

Cl^- (1.94 ± 0.92 μg m^{-3}), Na^+ (1.29 ± 0.48 μg m^{-3}), K^+ (0.63 ± 0.22 μg m^{-3}), and Mg^{2+} (0.22 ± 0.07 μg m^{-3}) (Figure S6a). The mass concentration of SNA accounted for 85.89% of the total water-soluble ions in $PM_{2.5}$. Comparing with the previous reports (Figure 4), the SNA concentrations were much lower than those collected in the western and northern polluted cities in winter, including Beijing (38.90, 22.70, and 22.4 μg m^{-3}, respectively) (Wang et al., 2015a), Xi'an (39.7, 21.43, and 12.50 μg m^{-3}, respectively) (Xu et al., 2016a), Wuhan (29.80, 29.80, and 16.80 μg m^{-3}, respectively) (Zhang et al., 2015) and Chengdu (31.80, 15.5, and 15.5 μg m^{-3}, respectively) (Tao et al., 2014a). However, the concentrations of SNA were higher than those collected in marine boundary layer, such as East China sea (29.80, 29.80, and 16.80 μg m^{-3}, respectively) (Nakamura et al., 2005), Northern South China Sea (7.80, 0.24, and 2.1 μg m^{-3}, respectively) (Zhang et al., 2007), South China sea (7.99, 0.08, and 1.083 μg m^{-3}, respectively) (Hsu et al., 2007), Taiwan Strait (5.20, 3.13, and 1.50 μg m^{-3}, respectively) (Li et al., 2016), and Tuoji island in Bohai Rim (8.90, 5.80, and 1.40 μg m^{-3}, respectively) (Zhang et al., 2014). The SNA levels in the YRC were close to Shanghai in winter (11.7, 13.33, and 8.11 μg m^{-3}, respectively) (Zhou et al., 2016). The mass ratio of NO_3^-/SO_4^{2-} was regarded as a marker to distinguish mobile source *vs.* stationary source (Huang et al., 2013). The ratio of NO_3^-/SO_4^{2-} in this campaign was also close to that of Shanghai, and lower than that in other cities (Figure 4), indicating that mobile source emissions (traffic) contributed the most to fine particles. Besides, the mass concentration of SO_4^{2-} definitely exceed the level of NO_3^- in the marine boundary layer (Figure 4), indicating that marine source was another important source for SO_4^{2-} (Calhoun et al., 1991). The average concentration of Ca^{2+}(2.23 μg m^{-3}) in this cruise was the highest among all locations and cruises (Figure 4), followed by Chengdu (2.10 μg m^{-3}), Wuhan (1.90 μg m^{-3}), and Xi'an (1.33 μg m^{-3}). As shown in Figure 4, Ca^{2+} also presented the higher concentration in the cities, and decreased from inland to coastal regions, indicating that Ca^{2+} was mainly from terrace crustal (Xiao et al., 2017). However, the concentrations of K^+ and Mg^{2+} for YRC were lower than those in the most samples among all location (Figure 4). K^+ may originate from BB, sea salt, and crustal dust. The average Cl^- concentration during YRC was also lower than those in most cities (Figure 4). However, Na^+ level in this cruise was higher than the most reported values (Figure 4). The poor correlation between Na^+ and Cl^- also indicated that two ions may have the different sources during YRC. Besides, the ratio of Cl^-/Na^+ among all location (Figure 4) were much higher than 1.17 (ratio of seawater), suggesting that anthropogenic sources, including BB and coal combustion, contributed the excessive Cl^- in China cities (Li et al., 2015a; Zhang et al., 2013). The concentration of levoglucosan, a BB tracer, ranged from 0.015-

0.18 μg m^{-3} with a mean value of 0.075 ± 0.047 μg m^{-3}, much higher than the average concentration of 0.0394 μg m^{-3} in Lin'an (30.3°N, 119.73°E) (a rural site in the YRD region) (Liang et al., 2017), indicating that BB was also a major contributor to $PM_{2.5}$ during YRC.

17 elements of $PM_{1.0}$ and $PM_{2.5}$ were measured, and the average concentrations are summarized in Table 3. For comparison, the data reported previously in the megacities (in winter) and the cruises are also outlined in Table 4. Ca show the highest concentration among all elements (Table 3) at all locations (Table 4), and shared 2.16% on average in $PM_{2.5}$, partly due to cold front with floating dust in this campaign. The secondary highest concentration among all elements was Fe (Table 3). This concentration (1.64 μg m^{-3}) in the campaign was higher than those at many urban sites, such as Beijing (1.55 μg m^{-3}) (Zhao et al., 2013c), Shanghai (0.56 μg m^{-3}) (Huang et al., 2012b), and Guangzhou (0.16 μg m^{-3}) (Lai et al., 2016), probably due to numerous steel industries/shipyards densely distributed on both banks of the Yangtze River. Other elements decreased from K (865.88 ng m^{-3}) to Tl (0.32 ng m^{-3}). Pb and Zn contributed the highest levels among heavy metals of $PM_{2.5}$. Except for inland cities, such as Beijing (Zhao et al., 2013c), Wuhan (Zhang et al., 2015), and Chengdu (Tao et al., 2014a), the average concentrations of Pb and Zn along the YRC were much higher than those in the other regions and cruises (Table 4). Both Pb and Zn could originate from coal combustion and/or mineral industry, which were related to energy structure and industrial layout over the MLYR region (Zhao et al., 2013c; Zhang et al., 2015; Tao et al., 2014a; Zhao et al., 2015).

The enrichment factors (EFs) were applied to distinguish crustal elements from the anthropogenic sources. The formula to evaluate EFs was:

$$EF_i = (X_i / X_R)_{\text{aerosol}} / (X'_i / X'_R)_{\text{crust}} \quad (3)$$

of which EF_i is the enrichment factor of element i; X_i and X_R are the concentrations of element i and reference element of R in aerosol, respectively; X'_i and X'_R are the background content of elements in the MLYR soil (Wei et al., 1991). Al was determined to originate from soil. Hence, it was selected as the reference element for the calculation. The elements of EFs < 10 included: Al, K, Mg, and Na, all of which were regarded from crustal or re-suspension local soil. The species with higher EFs (10 < EFs < 100) were thought to be the mixture of the crustal and anthropogenic sources, including Cr, Cu, Co, Ni, and V. Trace elements of EFs > 100, including Ca, Zn, Se, Pb, As, Mo, Fe, and Cd, were attributed to anthropogenic sources. To further explore sources of trace elements and potential geographical

distributions, PCA was used to classify the main source of trace elements of $PM_{2.5}$ using the rotate component matrix and PSCF for individual element was performed to infer the potential source and/or pathway regions. As shown in Figure 5a, trace elements were classified into four categories (PCA), which could explain 86.73% of the variance, indicating that the major sources of elements of $PM_{2.5}$ could be considered and explained. More specifically, the first component (component 1) could account for 38.48% of the variance, which was derived from coal combustion, including the high loadings of Cd, As, Pb, Tl, and Se. Particularly, Se was generally considered as a tracer for coal combustion, due to its formation in the high-temperature environment. Se produced by the rapid gas-to-particle conversion could undergo long-range transport (Nriagu, 1989; Wen and Carignan, 2007). As shown in Figure S6b, a significant correlation ($R^2 = 0.71$, $P < 0.01$) between SO_4^{2-} and Se also confirmed coal combustion. Furthermore, As and Pb mainly originated from coal combustion after phasing out of leaded gasoline in China since 1997 (Xu et al., 2012), both of which had significantly correlations with Se. The component 2 with a variation of 25.45%, contributed by the high loading of Al, Mg, Ca, and K, all of which obviously represented the crustal or soil elements, and showed the low EFs values (EFs< 10, except Ca). Component 3, accounting for 15.14% of the variation, was considered as the primary source of V, Co, and Ni. Both V and Ni were usually regarded as a tracer of heavy oil combustion (Zhao et al., 2013b; Becagli et al., 2017). The fourth component (component 4) showed the high loadings of Mn, Co, Zn, and Fe, all of which could explain 7.33% of the variance. Fe exhibited the high EFs value, indicating that these may originate from anthropogenic sources. Anthropogenic Fe was usually deemed to originate from steel factory and/or shipyard, both of which were densely distributed along the Yangtze River (Fu et al., 2014). Their chemical processes and potential source contributions would be detailed in section 3.4.

3.4 Regional difference in formation mechanism of aerosol pollution and potential source contributions of element in $PM_{2.5}$ over the MLYR region

3.4.1 Secondary component pollution related to coal combustion in central China

As illustrated in Figure 3, the mass concentrations of SNA with an average of 38.35 ± 15.17 μg/m^3 increased dramatically from coastal to inland cities and exhibited the highest level (#6, 79.06 μg/m^3) in Wuhan region (EP-4), accounting for nearly 50% of the local $PM_{2.5}$ mass loading. As mentioned above, SO_2 and NO_x also presented the high concentration in this region. Furthermore, Wuhan and the surrounding regions were controlled by a low-pressure system with the low wind speed and high RH

conditions (Figure S3), of which have been verified to cause haze episode (Zhao et al., 2013d; Quan et al., 2011; Wang et al., 2010). In addition, the ratio of NO_3^-/SO_4^{2-} in Wuhan area was close to the values of cities in northern China (relative low) (Figure 4), suggesting that the stationary sources (such as: coal-fired power station or stove emission) dominated in this region. Heavy clouds and high humidity in central China suggested aqueous phase transformation processes were probable the main reaction path of SO_4^{2-} from SO_2 (Wang et al., 2016; Zhao et al., 2013d). Besides, the mass fractions of SNA in $PM_{2.5}$ also peaked in the rural region (EP-2 and EP-6), which was in accord with the low ratio of T/B in these regions, suggesting that aerosol particles in the rural region were well aged.

Meanwhile, trace elements for coal combustion (component 1) had also the high concentration in EP-4 and EP-5 (Figure 5b) when the ship anchored in Wuhan and traveled through the Jiujiang area. As illustrated in Figure 6a-d, As, Cd, Pb, and Se showed the similar source distribution. The higher PSCF values in Hubei, Hunan, and Jiangxi provinces coincided well with the uneven regional distribution of the residential coal consumption (Figure S7) in central China, suggesting coal-related PM pollution was quite serious in this region during this cruise. The peak mass fraction of Cl^- and SO_4^{2-} in $PM_{2.5}$ in Wuhan was also confirmed this result Thus, it's concluded that coal combustion contributed significantly to serious pollution with the high SNA loading in Wuhan and the surrounding regions during sampling.

3.4.2 Mineral Dust in YRD region

Contrary to SNA distribution, the concentration of Ca^{2+} along this cruise increased from the mainland to the costal of East China Sea (Figure 3). The peak concentration of crustal elements (component 2) and Ca^{2+} mass fraction of $PM_{2.5}$ occurred in EP-7 when a cold front arrived and associated with northeast winds, accompanying with floating dust (Figure 3 and Figure 5b).In the Meantime, dust episode was verified by the MODIS true-color image on 2 and 3 December (Figure S4), further confirmed by a drastic decrease of RH with the prevailing northwest wind (Table 2 and Figure S3). As shown in Figure 6e-h, the YRD region and the Loess Plateau with the highest PSCF values were identified as the important source regions and/or pathways for crustal elements of Al, K, Mg and Ca. Meanwhile, the central China also showed the distribution of K and Mg, for which the coal combustion in this region could be primarily responsible. Furthermore, Ca showed the high EFs (EFs > 100), suggesting that the crustal element may not derive from natural source, but from anthropogenic re-suspension of road and/or construction activities along the Yangtze River. To further evaluate the impact of anthropogenic Ca, the equation below was applied:

$$Ca_{anthropogenic} = Ca_{total} - Al_{total} \times (Ca/Al)_{crust} \quad (4)$$

$(Ca/Al)_{crust}$ is the ratio of Ca to Al in the crust, and its value is 0.5. According to this method, the average $Ca_{anthropogenic}$ concentration was 2.15 μg m^{-3}, and the peak level reached to 3.42 μg m^{-3} on December 3. IF all of $Ca_{anthropogenic}$ in the samples of other cities and cruises (Table 4) were calculated according to the same method, its level in this cruise was much higher than those in other samples, suggesting that anthropogenic dust was dominated and distributed in the YRD region during the period.

Resembling Ca^{2+} distribution pattern, the maximum concentration and mass fraction of Na^+ and K^+ in $PM_{2.5}$ were also measured during EP-7. Significantly correlation between Ca^{2+} and K^+ suggested that dust could be the major source of K^+ in $PM_{2.5}$ sampled during YRC (Figure 3). In general, it's well known that dust particles with the high alkalinity could firstly neutralize SO_4^{2-} and NO_3^- in aerosol particles, then atmospheric ammonia was absorbed. The concentrations and mass fractions of SNA in $PM_{2.5}$ slightly increased at the end of the cruise (EP-7 and EP-8) (Figure 3) since carbonate in aerosol could enhance the uptake of acidic gases on particles (Huang et al., 2010). In the meanwhile, the increasing mass ratio of NO_3^-/SO_4^{2-} in EP-7 and EP-8 was attributed to two main reasons (Figure 3). The mobile sources (such as: vehicle emissions) increased and released a huge amount of NO_x when the vessel was close to the megacity (Huang et al., 2013). Furthermore, NO_2 could transform into NO_3^- via the heterogeneous process on dust aerosol surface (Nie et al., 2012).

3.4.3 Heavy metals in mega-city

Heavy metals have toxic effects on plants, animals, and human beings. However, there is no uniform stander concentration for control indicator (Sharma and Agrawal, 2005). The trace elements (component 3 and component 4), with highly EFs ranging from 24 to 1213, were considered to mainly come from heavy oil and industry, respectively. The high concentrations of V and Ni were observed when the ship berthed in the Waigaoqiao port berthing region of Shanghai (EP-8) (Figure 5b), where some field observations have also identified that heavy oil combustion exert a significant impact on the local air quality (Zhao et al., 2013b; Fu et al., 2014; Ding et al., 2017; Liu et al., 2017). It's also reported that the transition metals of Ni and V were greatly enriched in smaller particles with a diameter of < 1.0 μm (Jang et al., 2007). Fine particle Ni (Figure 6i) had almost same spatial distribution with Cr (Figure 6j), that Shanghai, Jiangsu, and the east of Anhui were identified as the major potential source regions and/or pathways, owing to ship emissions, nonferrous metal mining, and smelting industries. The Mongolian

plateau also was also the source region, indicating that nature dust may be another possible source for Cr and Ni. However, the high PSCF values of fine particle V were only derived from the YRD region and Mongolian plateau (Figure 6j). It's partly that V was considered to originate from heavy oil combustion, while Ni and Cr probably has other sources (Table S1) (Zhao et al., 2013b).

The temporal variations of component 4 peaked nearly in Wuhan and Shanghai (EP-4, EP-7, and EP-8) (Figure 5b) where China Baowu steel industry, and numerous shipyards were located in those regions (Ivošević et al., 2016). Fine particle Fe, Co, Mn, and Zn displayed similar regional distribution (Figure 6l-o), and the high PSCF levels were observed in the YRD region, indicating that steel industries and/or shipyards were densely distributed in East of Anhui, Jiangsu and Shanghai. Besides, the high PSCF value for Zn (Figure 6l) was also exhibited high value in Hubei, Henan, and Shanxi province, probably due to the influence of coal combustion and nonferrous metal smelting activities in these regions (Li et al., 2015b). Overall, it should be noted that anthropogenic sources in mega-cities (WNS) were dominant origins for trace elements in fine particles collected along this cruise.

3.4.4 Biomass burning in rural region

Numerous studies also have confirmed that levoglucosan mostly originate from BB (Liang et al., 2017; Ding et al., 2013b; Wan et al., 2017; Wang et al., 2014). The distribution of lev is irregular parabolic from inland to coastal areas in Figure 3. The maximum value of lev (0.18 μg m^{-3}) was observed in the rural of Anhui province (EP-6), while its level in YRD region (EP-8) was at very low levels. The elevated levels of CO and low-concentrations of SO_2 and NO_X also confirmed BB in EP6 and EP7 (Table 2). However, fire points couldn't be apparently observed in the satellite-detected fire maps (http://firefly.geog.umd.edu/firemap/), due to heavy cloud cover on 27 November and 1 December. During the whole observation periods, there was only one sample (#12, Figure S8) collected during BB event. It was verified by MODIS fire points, due to a cold front blowing heavy clouds away (Figure S4). The slightly higher lev concentration was observed in the night that was attributed to the lower boundary layer at night and BB for heating and cooking in the rural regions.

The levoglucosan concentration and ratio of OC to lev (OC/lev) were also widely applied to estimate the contribution of BB to OC in $PM_{2.5}$. An empirical model was utilized as proposed by Wan et al. (2017):

$$OC_{BB} = \left(\frac{[lev]}{[OC]}\right)_{ambient} / \left(\frac{[lev]}{[OC]}\right)_{BB} \quad (5)$$

The differences of the $(lev/OC)_{BB}$ ratio among different biomass fuels and combustion conditions were taken into account. So, the average $(lev/OC)_{BB}$ ratio of 8.14 % was selected to calculate the contribution of BB to OC (Wan et al., 2017). Figure S9 presents the variation of lev/OC ratio along the Yangtze River. The ratio of lev/OC during this cruise ranged from 0.03 % to 0.91 % with an average of 0.35 ± 0.24 %, which was comparable to that of Lin'an in YRD region (Liang et al., 2017). However, the ratio of lev/OC during YRC was near an order of magnitude of lower than its value in New Delhi (3.1 ± 0.8 %) (Li et al., 2014) and Lumbini (3.34 ± 2.53 %) in the northern edge of Indo-Gangetic Plain (Wan et al., 2017), where BB play an important role on air quality. Figure S9 also shows the time serious of contribution of BB-OC to OC. The average contribution of BB-OC/OC was 4.26 ± 2.89 %, while the mean mass fraction of OC to $PM_{2.5}$ was slightly higher than 20%. The peak contribution of OC deriving from BB to total OC of $PM_{2.5}$ nearly accounted for 11% in EP-6, which was approached that of the Pearl River region sites (13%) (Ho et al., 2014). Here, it's emphasized that our method based on empirical formula and value is just rough estimation. Hence, the radiocarbon measurement (^{14}C) of carbonaceous aerosol and air quality model simulation should need to confirm this result in the future.

3.5 Ship emission

3.5.1 Primary of ship emission

Over the past few decades, China's rapid economic development leads to the increasingly busy shipping transportation in the Yangtze River. However, there is lack of data related to ship emission along the stream of Yangtze River, especially in inland area. The ratio of V to Ni was used to judge whether ship emission could influence air quality (Isakson et al., 2001). The average ratio of V/Ni in the cruise is 1.27, which was in good agreement with the previous studies (Pandolfi et al., 2011; Zhang et al., 2014). Emission factors of heavy metals from different types of fuel oil were also analyzed in our group (Table S1). Only heavy oil contained V, while the V levels emitted from other diesel and petrol were under the detector limits. In this study, only V was regarded as the tracer for heavy oil combustion. However, it was still difficult to distinguish V from refinery and ship emission. Hence, the high-resolution back-trajectory and high-resolution of the ship position from the AIS data were applied to investigate ship plume during this cruise. As plotted in Figure 7, the numbers of the ship from AIS were closely related to the V concentrations. From the inland region to the East China Sea at Shanghai, the concentration of V of $PM_{2.5}$ generally increased, and reached the highest level of 0.06 μg m^{-3} on 4 December when the

vessel berthed in the anchorage of the Yangtze River estuary. Meanwhile, air masses in this evening originated from the port and anchorage (Figure S10). Hence, V of $PM_{2.5}$ sampled in the port of Shanghai could be probably attributable to ship emissions, especially from oceangoing vessels.

The contribution of primary ship emissions to $PM_{2.5}$ could be calculated by the equation developed by Agrawal et al. (2009):

$$PM_a = < \mathrm{a} > \times < r > \times V_a / < F_{V,HFO} > \quad (6)$$

where PM_a represents the primary $PM_{2.5}$ concentration estimated (μg m^{-3}); $< \mathrm{a} >$ is a coefficient of the fraction of V from ship emissions in fine particles in China (0.85), $< r >$ is average ratio of $PM_{2.5}$ to normalized V emitted (ppm); V_a represents the V amount of the samples (μg m^{-3}) during YRC, and is the V content of heavy oil on average from the vessels (ppm). The value of $< r >$ was set as 8205.8 ppm as Agrawal et al. (2009) reported. The value of $< F_{V,HFO} >$ was set as 65.3 ppm, of which represents of the average V contents (Zhao et al., 2013b). The average concentration of the primary ship emission was 1.01 ± 1.41 μg m^{-3}, ranging from 0.02 to 6.27 μg m^{-3}, which is higher than that at Tuoji Island (0.65 μg m^{-3}) (Zhang et al., 2014). The peak level of primary ship emission was observed in the Shanghai harbor.

3.5.2 Ship emission contribution to SO_4^{2-}, NO_3^-, and OC

To in-depth characterize the contribution of the ship emissions to secondary fine particles, a lower limit of the SO_4^{2-}/V, NO_3^-/V, EC/V, and OC/V ratios (equal to the average minus one standard deviation) was applied to estimate the particulate from heavy oil combustion in the course of the Yangtze River (Becagli et al., 2017). As presented in Figure S11a-b, the mass ratio of SO_4^{2-}/V and NO_3^-/V decreased rapidly with increasing V concentration. According to ship traffic numbers, weather condition, and the emission factors of different type oils (Table S1), the samples with V > 15 ng m^{-3} were mainly considered to come from ship emissions.

The limit ratio of SO_4^{2-}/V, NO_3^-/V and OC/V, and the estimation of ship emissions contributions to SO_4^{2-}, NO_3^-, OC, and $PM_{2.5}$ are summarized in Table S2 in supporting information. The minimum ratio of NO_3^-/V in this cruise was nearly twice greater than the limit ratio for SO_4^{2-}/V, which was contrary to the previous results with higher SO_4^{2-} from ship emissions observed in summer on the island of Lampedusa (35.5°N, 12.6°E) in the central Mediterranean. In general, SO_4^{2-} and NO_3^- in aerosol were mainly formed

through gas precursors of SO_2 and NO_X, respectively, both of which were completely different for lift-time and chemical processes in the atmosphere. High UV radiation and humidity could accurate the reaction rate of SO_2 to SO_4^{2-} (Zhou et al., 2016). However, NO_3^- was in gas-aerosol equilibrium with gaseous HNO_3 (g). Low temperature and humidity would shift the gas-aerosol equilibrium to the particle phase (NO_3^-) (Matthias et al., 2010; Wang et al., 2016). One reason for this discrepancy was probably meteorological and photochemical conditions, which leaded to lower sulfur conversion rate, and particulate NO_3^- domination in the low temperature and moisture in winter during this cruise (Table 2). On the other hand, NO_3^- may have other sources in Shanghai port, whereas Lampedusa was a remote site (Becagli et al., 2017). The average estimated concentration of minimum SO_4^{2-} derived from ship emission was 1.38 μg m^{-3} during YRC, which was similar to the value (1.35 μg m^{-3}) measured in the Mediterranean (Becagli et al., 2017; Becagli, 2012).

EC and OC were also estimated by the same methods for SO_4^{2-} and NO_3^-, and the lower limit for OC/V and EC/V ratio are also presented in Figure S11c-d. Besides, significant correlation between V and EC (R^2 = 0.71, P < 0.01) suggested that V and EC have same sources (Agrawal et al., 2009). In this cruise, organic matter (OM) of $PM_{2.5}$ were estimated from OC by multiplying a conversion factor of 1.4, due to typical fresh emission and weak light in winter (Becagli et al., 2017). The estimated lower limit for average of ship emissions was 7.65 μg m^{-3}, nearly occupying 6.41% of $PM_{2.5}$ during YRC. The peak ship contribution could reach to 36.04% of total $PM_{2.5}$ when the vessel berthed in the Waigaoqiao port of Shanghai, which was slight above the value (20-30%) estimated by Liu et al. (2017) during ship-plume-influenced periods. It should be noted that the ship emission decreased from Shanghai port to the inland area. One reason for this was correspond to the density of ship in the Yangtze River channel. On the other hand, fuel oils were completely different between the ship travelling in inland waterway and the oceangoing vessel. In general, light diesel with low EFs of heavy metals (such as: V, Ni) was widely used by the ships on river, whereas heavy oil showing high content of V and Ni were widely burned onboard marine vessels as fuel (Table S1). Oceangoing ship emissions were probably the major air pollution sources in the Shanghai port. Hence, it is urgent to establish emission control areas (ECAs) in Shanghai ports. However, it is worth noting that our estimation based on empirical values was also limited by meteorological conditions and sample numbers. Hence, long-term observation and high resolutions model simulation of ship emissions should be strengthened as part of control of air quality along the Yangtze River, especially in Shanghai harbor cluster.

4 Conclusion

In order to better characterize air quality over the region of MLYR, an intensive atmospheric observation was conducted during YRC. A shipboard measurement was conducted to measure and analysis an suite of air pollutants (trace gases and fine particles) in this region. The average concentrations of $PM_{1.0}$ and $PM_{2.5}$ were 96.69 ± 22.18 μg m^{-3} and 119.29 ± 33.67 μg m^{-3} during the cruise, respectively. The most abundant ionic species in $PM_{2.5}$ was SO_4^{2-} with an average concentration of 15.21 ± 6.69 μg/m^3, followed by NO_3^- (13.76 ± 4.99μg/m^3), NH_4^+ (9.38 ± 4.35μg/m^3), Ca^{2+} (2.23 ± 1.24μg/m^3), Cl^- (1.94 ± 0.92 μg m^{-3}), Na^+ (1.29 ± 0.48 μg m^{-3}), K^+ (0.63 ± 0.22 μg m^{-3}), and Mg^{2+} (0.22 ± 0.07 μg m^{-3}), respectively. Combined with satellite data, back trajectory, principal component analysis (PCA), and potential source contribution function (PSCF), major chemical composition of $PM_{2.5}$ manifested greatly geographical differences and diverse anthropogenic emission sources from coastal to inland regions. Wuhan suffered secondary aerosol pollution with SNA accounting for nearly 50% of $PM_{2.5}$. The significant correlation between Se and SO_4^{2-} revealed that the stationary emissions may play an important role in SNA formation. The concentrations of levoglucosan of $PM_{2.5}$ and CO column levels from the satellite data significantly enhanced in the rural areas (Anhui and Jiangxi), indicating that BB from the both shores of the Yangtze River may make remarkable contribution to air pollution in rural area during YRC. Further, the crustal elements of Al and Ca presented the high levels in the YRD regions and the high value of enrichment factors (EFs) of Ca (EFs > 100) coupling with the PSCF results suggested the crustal elements may derive from re-suspension of dust from road and/or construction activity along the banks of the Yangtze River. Ship emissions displayed a significant effect on air pollution, and could contribute to more than 36% of $PM_{2.5}$ in the ports of Shanghai. As far as we know, it's the first comprehensive observation of air quality over the MLYR region using a vessel mobile platform. The results herein suggested that the differentiated control measures in accordance with local pollution characteristics should be taken to tackle air pollution.

Competing interests

The authors claim that they have no competing interests.

Acknowledgements

This work was supported by the Ministry of Science and Technology of China (No. 2016YFC0202700, 2014BAC22B00), the National Natural Science Foundation of China (No. 91743202, 21527814) and Marie Skłodowska-Curie Actions (690958-MARSU-RISE-2015).

References:

Ackerman, A. S., Kirkpatrick, M. P., Stevens, D. E., and Toon, O. B.: The impact of humidity above stratiform clouds on indirect aerosol climate forcing, Nature, 432, 1014, 2004.

Agrawal, H., Eden, R., Zhang, X., Fine, P. M., Katzenstein, A., Miller, J. W., Ospital, J., and Teffera, S.: Primary particulate matter from ocean-going engines in the Southern California Air Basin, Environ. Sci. Technol., 43, 5398-5402, 2009.

An, J., Wang, H., Shen, L., Zhu, B., Zou, J., Gao, J., and Kang, H.: Characteristics of new particle formation events in Nanjing, China: Effect of water-soluble ions, Atmos. Environ., 108, 32-40, 10.1016/j.atmosenv.2015.01.038, 2015.

Baltrenas, P., Baltrenaite, E., Sereviciene, V., and Pereira, P.: Atmospheric BTEX concentrations in the vicinity of the crude oil refinery of the Baltic region, Environ. Monit. Assess., 182, 115-127, 2011.

Becagli, S., Anello, F., Bommarito, C., Cassola, F., Calzolai, G., Di Iorio, T., di Sarra, A., Gómez-Amo, J.-L., Lucarelli, F., Marconi, M., Meloni, D., Monteleone, F., Nava, S., Pace, G., Severi, M., Sferlazzo, D. M., Traversi, R., and Udisti, R.: Constraining the ship contribution to the aerosol of the central Mediterranean, Atmos. Chem. Phys., 17, 2067-2084, 10.5194/acp-17-2067-2017, 2017.

Becagli, S. S., D. M.Pace, G.di Sarra, A.Bommarito, C.Calzolai, G.Ghedini, C.Lucarelli, F.Meloni, D.Monteleone, F.Severi, M.Traversi, R.Udisti, R.: Evidence for heavy fuel oil combustion aerosols from chemical analyses at the island of Lampedusa: a possible large role of ships emissions in the Mediterranean, Atmos. Chem. Phys., 12, 3479-3492, 10.5194/acp-12-3479-2012, 2012.

Boreddy, S. K. R., and Kawamura, K.: A 12-year observation of water-soluble ions in TSP aerosols collected at a remote marine location in the western North Pacific: an outflow region of Asian dust, Atmos. Chem. Phys., 15, 6437-6453, 10.5194/acp-15-6437-2015, 2015.

Calhoun, J. A., Bates, T. S., and Charlson, R. J.: Sulfur isotope measurements of submicrometer sulfate aerosol particles over the Pacific Ocean, Geophys. Res. Lett., 18, 1877-1880, 10.1029/91gl02304, 1991.

Chameides, W. L., Yu, H., Liu, S. C., Bergin, M., Zhou, X., Mearns, L., Wang, G., Kiang, C. S., Saylor, R. D., and Luo, C.: Case study of the effects of atmospheric aerosols and regional haze on agriculture: an opportunity to enhance crop yields in China through emission controls?, Proc. Nat. Acad. Sci. U.S.A., 96, 13626-13633, 1999.

Cheng, Z., Wang, S., Fu, X., Watson, J. G., Jiang, J., Fu, Q., Chen, C., Xu, B., Yu, J., and Chow, J. C.: Impact of biomass burning on haze pollution in the Yangtze River delta, China: a case study in summer

612 2011, Atmos. Chem. Phys., 14, 4573-4585, 10.5194/acp-14-4573-2014, 2014.
613 Coggon, M. M., Sorooshian, A., Wang, Z., Metcalf, A. R., Frossard, A. A., Lin, J. J., Craven, J. S., Nenes,
614 A., Jonsson, H. H., Russell, L. M., Flagan, R. C., and Seinfeld, J. H.: Ship impacts on the marine
615 atmosphere: insights into the contribution of shipping emissions to the properties of marine aerosol and
616 clouds, Atmos. Chem. Phys., 12, 8439-8458, 10.5194/acp-12-8439-2012, 2012.
617 Ding, A. J., Fu, C. B., Yang, X. Q., Sun, J. N., Petäjä, T., Kerminen, V. M., Wang, T., Xie, Y., Herrmann,
618 E., and Zheng, L. F.: Intense atmospheric pollution modifies weather: a case of mixed biomass burning
619 with fossil fuel combustion pollution in eastern China, Atmos. Chem. Phys., 13, 10545-10554,
620 10.5194/acp-13-10545-2013, 2013a.
621 Ding, X., Wang, X., Xie, Z., Zhang, Z., and Sun, L.: Impacts of Siberian biomass burning on organic
622 aerosols over the North Pacific Ocean and the Arctic: primary and secondary organic tracers, Environ.
623 Sci. Technol., 47, 3149-3157, 2013b.
624 Ding, X., Kong, L., Du, C., Zhanzakova, A., Wang, L., Fu, H., Chen, J., Yang, X., and Cheng, T.: Long-
625 range and regional transported size-resolved atmospheric aerosols during summertime in urban Shanghai,
626 Sci. Total Environ., 583, 334-343, 2017.
627 Draxler, R. R., and Hess, G. D.: An overview of the HYSPLIT_4 modelling system for trajectories, Aust.
628 Meteorol. Mag., 47, 295-308, 1998.
629 Fan, Q., Zhang, Y., Ma, W., Ma, H., Feng, J., Yu, Q., Yang, X., Ng, S. K., Fu, Q., and Chen, L.: Spatial
630 and Seasonal Dynamics of Ship Emissions over the Yangtze River Delta and East China Sea and Their
631 Potential Environmental Influence, Environ. Sci. Technol., 50, 1322-1329, 2016.
632 Fu, H. B., Shang, G. F., Lin, J., Hu, Y. J., Hu, Q. Q., Guo, L., Zhang, Y. C., and Chen, J. M.: Fractional
633 iron solubility of aerosol particles enhanced by biomass burning and ship emission in Shanghai, East
634 China, Sci. Tot. Environ., 481, 377-391, 2014.
635 Fu, X., Wang, S., Zhao, B., Xing, J., Cheng, Z., Liu, H., and Hao, J.: Emission inventory of primary
636 pollutants and chemical speciation in 2010 for the Yangtze River Delta region, China, Atmos. Environ.,
637 70, 39-50, 2013.
638 Gaston, C. J., Quinn, P. K., Bates, T. S., Gilman, J. B., Bon, D. M., Kuster, W. C., and Prather, K. A.:
639 The impact of shipping, agricultural, and urban emissions on single particle chemistry observed aboard
640 the R/V Atlantis during CalNex, J. Geophys. Res. Atmos., 118, 5003-5017, 10.1002/jgrd.50427, 2013.
641 Geng, F., Zhang, Q., Tie, X., Huang, M., Ma, X., Deng, Z., Yu, Q., Quan, J., and Zhao, C.: Aircraft

measurements of O3, NOx, CO, VOCs, and SO2 in the Yangtze River Delta region, Atmos. Environ., 43, 584-593, 2009.

Girach, I., Nair, V. S., Babu, S. S., and Nair, P. R.: Black carbon and carbon monoxide over Bay of Bengal during W_ICARB: Source characteristics, Atmos. Environ., 94, 508-517, 2014.

Han, T., Qiao, L., Zhou, M., Qu, Y., Du, J., Liu, X., Lou, S., Chen, C., Wang, H., and Zhang, F.: Chemical and optical properties of aerosols and their interrelationship in winter in the megacity Shanghai of China, J. Environ. Sci., 27, 59-69, 2015.

Han, Y.-J., Holsen, T. M., Hopke, P. K., and Yi, S.-M.: Comparison between back-trajectory based modeling and Lagrangian backward dispersion modeling for locating sources of reactive gaseous mercury, Environ. Sci. Technol., 39, 1715-1723, 2005.

He, Q., Li, C., Geng, F., Yang, H., Li, P., Li, T., Liu, D., and Pei, Z.: Aerosol optical properties retrieved from Sun photometer measurements over Shanghai, China, J. Geophys. Res. Atmos., 117, D16204, 10.1029/2011jd017220, 2012.

Ho, K. F., Engling, G., Sai Hang Ho, S., Huang, R., Lai, S., Cao, J., and Lee, S. C.: Seasonal variations of anhydrosugars in PM2.5 in the Pearl River Delta Region, China, Tellus B: Chemical and Physical Meteorology, 66, 22577, 10.3402/tellusb.v66.22577, 2014.

Hopke, P. K., Barrie, L. A., Li, S. M., Cheng, M. D., Li, C., and Xie, Y.: Possible sources and preferred pathways for biogenic and non-sea-salt sulfur for the high Arctic, J. Geophys. Res. Atmos., 100, 16595-16603, 10.1029/95JD01712, 1995.

Hsu, S.-C., Liu, S. C., Kao, S.-J., Jeng, W.-L., Huang, Y.-T., Tseng, C.-M., Tsai, F., Tu, J.-Y., and Yang, Y.: Water-soluble species in the marine aerosol from the northern South China Sea: High chloride depletion related to air pollution, J. Geophys. Res., 112, 10.1029/2007jd008844, 2007.

Huang, K., Zhuang, G., Lin, Y., Fu, J. S., Wang, Q., Liu, T., Zhang, R., Jiang, Y., Deng, C., and Fu, Q.: Typical types and formation mechanisms of haze in an Eastern Asia megacity, Shanghai, Atmos. Chem. Phys., 12, 105, 10.5194/acp-12-105-2012, 2012a.

Huang, K., Zhuang, G., Lin, Y., Wang, Q., Fu, J. S., Zhang, R., Li, J., Deng, C., and Fu, Q.: Impact of anthropogenic emission on air quality over a megacity–revealed from an intensive atmospheric campaign during the Chinese Spring Festival, Atmos. Chem. Phys., 12, 11631-11645, 10.5194/acp-12-11631-2012, 2012b.

Huang, K., Zhuang, G., Lin, Y., Wang, Q., Fu, J. S., Fu, Q., Liu, T., and Deng, C.: How to improve the

672 air quality over megacities in China: pollution characterization and source analysis in Shanghai before,
673 during, and after the 2010 World Expo, Atmos. Chem. Phys., 13, 5927-5942, 10.5194/acp-13-5927-2013,
674 2013.
675 Isakson, J., Persson, T. A., and Lindgren, E. S.: Identification and assessment of ship emissions and their
676 effects in the harbour of Göteborg, Sweden, Atmos. Environ., 35, 3659-3666, 2001.
677 Ivošević, T., Stelcer, E., Orlić, I., Bogdanović Radović, I., and Cohen, D.: Characterization and source
678 apportionment of fine particulate sources at Rijeka, Croatia from 2013 to 2015, Nucl. Instrum. Methods.
679 Phys. Res. B., 371, 376-380, 2016.
680 Jalkanen, J., Johansson, L., and Kukkonen, J.: A comprehensive inventory of ship traffic exhaust
681 emissions in the European sea areas in 2011, Atmos. Chem. Phys., 16, 71-84, 2015.
682 Jang, H. N., Lee, S. J. H., Hwang, K. W., Yoo, J. I., Sok, C. H., and Kim, S. H.: Formation of fine
683 particles enriched by V and Ni from heavy oil combustion: Anthropogenic sources and drop-tube furnace
684 experiments, Atmos. Environ., 41, 1053-1063, 2007.
685 Jones, A. D. L. A., Roberts, D. L., and Slingo, A.: A climate model study of indirect radiative forcing by
686 anthropogenic sulphate aerosols, Nature, 370, 450-453, 1994.
687 Kang, H., Zhu, B., Su, J., Wang, H., Zhang, Q., and Wang, F.: Analysis of a long-lasting haze episode in
688 Nanjing, China, Atmos. Res., 78-87, 2013a.
689 Kang, H., Zhu, B., Su, J., Wang, H., Zhang, Q., and Wang, F.: Analysis of a long-lasting haze episode in
690 Nanjing, China, Atmos. Res., 120-121, 78-87, 2013b.
691 Kerminen, V.-M., Hillamo, R., Teinilä, K., Pakkanen, T., Allegrini, I., and Sparapani, R.: Ion balances
692 of size-resolved tropospheric aerosol samples: implications for the acidity and atmospheric processing
693 of aerosols, Atmos. Environ., 35, 5255-5265, 2001.
694 Kong, S., Li, X., Li, L., Yin, Y., Chen, K., Yuan, L., Zhang, Y., Shan, Y., and Ji, Y.: Variation of
695 polycyclic aromatic hydrocarbons in atmospheric PM2.5 during winter haze period around 2014 Chinese
696 Spring Festival at Nanjing: Insights of source changes, air mass direction and firework particle injection,
697 Sci. Tot. Environ., 520, 59-72, 2015.
698 Lai, S., Zhao, Y., Ding, A., Zhang, Y., Song, T., Zheng, J., Ho, K. F., Lee, S.-c., and Zhong, L.:
699 Characterization of PM2.5 and the major chemical components during a 1-year campaign in rural
700 Guangzhou, Southern China, Atmos. Res., 167, 208-215, 2016.
701 Li, C., Ma, Z., Chen, J., Wang, X., Ye, X., Wang, L., Yang, X., Kan, H., Donaldson, D. J., and Mellouki,

A.: Evolution of biomass burning smoke particles in the dark, Atmos. Environ., 120, 244-252, 2015a.

Li, J., Wang, G., Aggarwal, S. G., Huang, Y., Ren, Y., Zhou, B., Singh, K., Gupta, P. K., Cao, J., and Zhang, R.: Comparison of abundances, compositions and sources of elements, inorganic ions and organic compounds in atmospheric aerosols from Xi'an and New Delhi, two megacities in China and India, Sci. Total Environ., 476-477, 485-495, 10.1016/j.scitotenv.2014.01.011, 2014.

Li, T.-C., Yuan, C.-S., Hung, C.-H., Lin, H.-Y., Huang, H.-C., and Lee, C.-L.: Chemical Characteristics of Marine Fine Aerosols over Sea and at Offshore Islands during Three Cruise Sampling Campaigns in the Taiwan Strait– Sea Salts and Anthropogenic Particles, Atmos. Chem. Phys. Discuss., 1-27, 10.5194/acp-2016-384, 2016.

Li, T., Wang, Y., Li, W. J., Chen, J. M., Wang, T., and Wang, W. X.: Concentrations and solubility of trace elements in fine particles at a mountain site, southern China: regional sources and cloud processing, Atmos. Chem. Phys., 15, 8987-9002, 10.5194/acp-15-8987-2015, 2015b.

Liang, L., Engling, G., Zhang, X., Sun, J., Zhang, Y., Xu, W., Liu, C., Zhang, G., Liu, X., and Ma, Q.: Chemical characteristics of PM2.5 during summer at a background site of the Yangtze River Delta in China, Atmos. Res., 198, 163-172, 2017.

Liao, T., Wang, S., Ai, J., Gui, K., Duan, B., Zhao, Q., Zhang, X., Jiang, W., and Sun, Y.: Heavy pollution episodes, transport pathways and potential sources of PM2.5 during the winter of 2013 in Chengdu (China), Sci. Total Environ., 584, 1056-1065, 2017.

Lin, J. T.: Satellite constraint for emissions of nitrogen oxides from anthropogenic, lightning and soil sources over East China on a high-resolution grid, Atmos. Chem. Phys., 11, 29807-29843, 10.5194/acp-12-2881-2012, 2011.

Liu, Z., Lu, X., Feng, J., Fan, Q., Zhang, Y., and Yang, X.: Influence of Ship Emissions on Urban Air Quality: A Comprehensive Study Using Highly Time-Resolved Online Measurements and Numerical Simulation in Shanghai, Environ. Sci. Technol., 51, 202-211, 2017.

Matthias, V., Bewersdorff, I., Aulinger, A., and Quante, M.: The contribution of ship emissions to air pollution in the North Sea regions, Environ. Pollut., 158, 2241-2250, 10.1016/j.envpol.2010.02.013, 2010.

Moldanová, J., Fridell, E., Popovicheva, O., Demirdjian, B., Tishkova, V., Faccinetto, A., and Focsa, C.: Characterisation of particulate matter and gaseous emissions from a large ship diesel engine, Atmos. Environ., 43, 2632-2641, 2009.

Nakamura, T., Matsumoto, K., and Uematsu, M.: Chemical characteristics of aerosols transported from Asia to the East China Sea: an evaluation of anthropogenic combined nitrogen deposition in autumn, Atmos. Environ., 39, 1749-1758, 2005.

Novakov, T., and Penner, J. E.: Large contribution of organic aerosols to cloud-condensation-nuclei concentrations, Nature, 365, 823-826, 1993.

Nriagu, J. O.: A global assessment of natural sources of atmospheric trace metals, Nature, 338, 47-49, 1989.

Pandis, S. N., Capaldo, K., Corbett, J. J., Kasibhatla, P., and Fischbeck, P.: Effects of ship emissions on sulphur cycling and radiative climate forcing over the ocean, Nature, 400, 743-746, 1999.

Pandolfi, M., Gonzalez-Castanedo, Y., Alastuey, A., Jd, D. L. R., Mantilla, E., As, D. L. C., Querol, X., Pey, J., Amato, F., and Moreno, T.: Source apportionment of PM10 and PM2.5 at multiple sites in the strait of Gibraltar by PMF: impact of shipping emissions, Environ Sci Pollut Res, 18, 260-269, 2011.

Pöschl, U.: Atmospheric aerosols: composition, transformation, climate and health effects, Angew. Chem. Int. Ed., 44, 7520-7540, 2005.

Quan, J., Zhang, Q., He, H., Liu, J., Huang, M., and Jin, H.: Analysis of the formation of fog and haze in North China Plain (NCP), Atmos. Chem. Phys., 11, 8205-8214, 10.5194/acp-11-8205-2011, 2011.

Seaton, A., Godden, D., MacNee, W., and Donaldson, K.: Particulate air pollution and acute health effects, The lancet, 345, 176-178, 1995.

Sharma, R. K., and Agrawal, M.: Biological effects of heavy metals: An overview, J. Environ. Biol., 26, 301, 2005.

Shen, G. F., Yuan, S. Y., Xie, Y. N., Xia, S. J., Li, L., Yao, Y. K., Qiao, Y. Z., Zhang, J., Zhao, Q. Y., and Ding, A. J.: Ambient levels and temporal variations of PM2.5 and PM10 at a residential site in the mega-city, Nanjing, in the western Yangtze River Delta, China, Journal of Environmental Science and Health, Part A, 49, 171-178, 2014.

Stier, P., Feichter, J., Kinne, S., Kloster, S., Vignati, E., Wilson, J., Ganzeveld, L., Tegen, I., Werner, M., and Balkanski, Y.: The aerosol-climate model CHAM5-HAM, Atmos. Chem. Phys., 5, 1125-1156, 10.5194/acp-5-1125-2005 2005.

Sun, X., Luo, X., Yan, C., Zhen, Z., Xu, J., Zhang, D., Suo, C., and Ding, Y.: Spatio-temporal characteristics of air pollution in Nanjing during 2013 to 2016 under the pollution control and meteorological factors, J. Environ. Earth., 8, 506-515, 2017.

762 Tao, J., Gao, J., Zhang, L., Zhang, R., Che, H., Zhang, Z., Lin, Z., Jing, J., Cao, J., and Hsu, S. C.: PM2.5
763 pollution in a megacity of southwest China: source apportionment and implication, Atmos. Chem. Phys.,
764 14, 8679-8699, 10.5194/acp-14-8679-2014, 2014a.
765 Tao, Y., Yin, Z., Ye, X., Ma, Z., and Chen, J.: Size distribution of water-soluble inorganic ions in urban
766 aerosols in Shanghai, Atmos. Pollut. Res., 5, 639-647, 2014b.
767 Wan, X., Kang, S., Li, Q., Rupakheti, D., Zhang, Q., Guo, J., Chen, P., Tripathee, L., Rupakheti, M.,
768 Panday, A. K., Wang, W., Kawamura, K., Gao, S., Wu, G., and Cong, Z.: Organic molecular tracers in
769 the atmospheric aerosols from Lumbini, Nepal, in the northern Indo-Gangetic Plain: influence of biomass
770 burning, Atmos. Chem. Phys., 17, 8867-8885, 10.5194/acp-17-8867-2017, 2017.
771 Wang, G., Zhang, R., Gomez, M. E., Yang, L., Levy Zamora, M., Hu, M., Lin, Y., Peng, J., Guo, S.,
772 Meng, J., Li, J., Cheng, C., Hu, T., Ren, Y., Wang, Y., Gao, J., Cao, J., An, Z., Zhou, W., Li, G., Wang,
773 J., Tian, P., Marrero-Ortiz, W., Secrest, J., Du, Z., Zheng, J., Shang, D., Zeng, L., Shao, M., Wang, W.,
774 Huang, Y., Wang, Y., Zhu, Y., Li, Y., Hu, J., Pan, B., Cai, L., Cheng, Y., Ji, Y., Zhang, F., Rosenfeld,
775 D., Liss, P. S., Duce, R. A., Kolb, C. E., and Molina, M. J.: Persistent sulfate formation from London
776 Fog to Chinese haze, Proc. Natl. Acad. Sci. U.S.A, 113, 13630-13635, 2016.
777 Wang, H., Lou, S., Huang, C., Qiao, L., Tang, X., Chen, C., Zeng, L., Wang, Q., Zhou, M., and Lu, S.:
778 Source Profiles of Volatile Organic Compounds from Biomass Burning in Yangtze River Delta, China,
779 Aerosol. Air. Qual. Res., 14, 818–828, 2014.
780 Wang, H., Tian, M., Li, X., Chang, Q., Cao, J., Yang, F., Ma, Y., and He, K.: Chemical Composition and
781 Light Extinction Contribution of PM2.5 in Urban Beijing for a 1-Year Period, Aerosol Air Qual. Res, 15,
782 2200-2211, 2015a.
783 Wang, H. L., Qiao, L. P., Lou, S. R., Zhou, M., Chen, J. M., Wang, Q., Tao, S. K., Chen, C. H., Huang,
784 H. Y., Li, L., and Huang, C.: PM2.5 pollution episode and its contributors from 2011 to 2013 in urban
785 Shanghai, China, Atmos. Environ., 123, 298-305, 2015b.
786 Wang, S., Yu, S., Yan, R., Zhang, Q., Li, P., Wang, L., Liu, W., and Zheng, X.: Characteristics and
787 origins of air pollutants in Wuhan, China, based on observations and hybrid receptor models, J. Air Waste
788 Manage. Assoc., 67, 739-753, 10.1080/10962247.2016.1240724, 2017.
789 Wang, T., Nie, W., Gao, J., Xue, L. K., Gao, X. M., Wang, X. F., Qiu, J., Poon, C. N., .Meinardi, S.,
790 Blake, D., Wang, S. L., Ding, A. J., Chai, F. H., Zhang, Q. Z., and Wang, W. X.: Air quality during the
791 2008 Beijing Olympics: secondary pollutants and regional impact, Atmos. Chem. Phys., 10, 7603-7615,

10.5194/acp-10-7603-2010, 2010.

Wang, X., Bi, X., Sheng, G., and Fu, J.: Hospital indoor PM10/PM2.5 and associated trace elements in Guangzhou, China, Sci. Total Environ., 366, 124-135, 10.1016/j.scitotenv.2005.09.004, 2006.

Wang, X., Miao, Y., Zhang, Y., Li, Y., Wu, M., and Yu, G.: Primary sources and secondary formation of organic aerosols in Beijing, China, Environ. Sci. Technol., 46, 9846-9853, 2012.

Wang, Y. Q., Zhang, X. Y., and Draxler, R. R.: TrajStat: GIS-based software that uses various trajectory statistical analysis methods to identify potential sources from long-term air pollution measurement data, Environ. Model. Software, 24, 938-939, 2009.

Wei, F., Chen, J., Wu, Y., and Zheng, C.: Study of the background contents of 61 elements of soils in China, Environmental Science, 12, 12-19, 1991

Wen, H., and Carignan, J.: Reviews on atmospheric selenium: Emissions, speciation and fate, Atmos. Environ., 41, 7151-7165, 2007.

Xiao, H., Xiao, H., Luo, L., Shen, C., Long, A., Chen, L., Long, Z., and Li, D.: Atmospheric aerosol compositions over the South China Sea: temporal variability and source apportionment, Atmos. Chem. Phys., 17, 3199-3214, 10.5194/acp-17-3199-2017, 2017.

Xu, H., Cao, J., Chow, J. C., Huang, R.-J., Shen, Z., Chen, L. A., Ho, K. F., and Watson, J. G.: Inter-annual variability of wintertime PM2.5 chemical composition in Xi'an, China: Evidences of changing source emissions, Sci. Tot. Environ., 545, 546-555, 2016a.

Xu, H. M., Cao, J. J., Ho, K. F., Ding, H., Han, Y. M., Wang, G. H., Chow, J. C., Watson, J. G., Khol, S. D., Qiang, J., and Li, W. T.: Lead concentrations in fine particulate matter after the phasing out of leaded gasoline in Xi'an, China, Atmos. Environ., 46, 217-224, 2012.

Xu, W. Y., Zhao, C. S., Ran, L., Deng, Z. Z., Liu, P. F., Ma, N., Lin, W. L., Xu, X. B., Yan, P., He, X., Yu, J., Liang, W. D., and Chen, L. L.: Characteristics of pollutants and their correlation to meteorological conditions at a suburban site in the North China Plain, Atmos. Chem. Phys., 11, 4353-4369, 10.5194/acp-11-4353-2011, 2011.

Xu, X., Zhao, T., Liu, F., Gong, S. L., Kristovich, D., Lu, C., Guo, Y., Cheng, X., Wang, Y., and Ding, G.: Climate modulation of the Tibetan Plateau on haze in China, Atmos. Chem. Phys., 16, 1365-1375, 10.5194/acp-16-1365-2016, 2016b.

Zhan, J., Gao, Y., Li, W., Chen, L., Lin, H., and Lin, Q.: Effects of ship emissions on summertime aerosols at Ny–Alesund in the Arctic, Atmos. Pollut. Res., 5, 500-510, 2014.

822 Zhang, F., Chen, Y., Tian, C., Wang, X., Huang, G., Fang, Y., and Zong, Z.: Identification and
823 quantification of shipping emissions in Bohai Rim, China, Sci. Tot. Environ., 497, 570-577, 2014.
824 Zhang, F., Wang, Z., Cheng, H., Lv, X., Gong, W., Wang, X., and Zhang, G.: Seasonal variations and
825 chemical characteristics of PM2.5 in Wuhan, central China, Sci. Tot. Environ., 518, 97-105, 2015.
826 Zhang, F., Chen, Y., Tian, C., Lou, D., Li, J., Zhang, G., and Matthias, V.: Emission factors for gaseous
827 and particulate pollutants from offshore diesel engine vessels in China, Atmos. Chem. Phys., 16, 6319-
828 6334, 10.5194/acp-16-6319-2016, 2016.
829 Zhang, M., Wang, X., Chen, J., Cheng, T., Wang, T., Yang, X., Gong, Y., Geng, F., and Chen, C.:
830 Physical characterization of aerosol particles during the Chinese New Year's firework events, Atmos.
831 Environ., 44, 5191-5198, 2010.
832 Zhang, R., Jing, J., Tao, J., Hsu, S. C., Wang, G., Cao, J., Lee, C. S. L., Zhu, L., Chen, Z., Zhao, Y., and
833 Shen, Z.: Chemical characterization and source apportionment of PM2.5 in Beijing: seasonal perspective,
834 Atmos. Chem. Phys., 13, 7053-7074, 10.5194/acp-13-7053-2013, 2013.
835 Zhang, X., Zhuang, G., Guo, J., Yin, K., and Zhang, P.: Characterization of aerosol over the Northern
836 South China Sea during two cruises in 2003, Atmos. Environ., 41, 7821-7836, 2007.
837 Zhao, B., Wang, S. X., Liu, H., Xu, J. Y., Fu, K., Klimont, Z., Hao, J. M., He, K. B., Cofala, J., and
838 Amann, M.: NOx emissions in China: historical trends and future perspectives, Atmos. Chem. Phys., 13,
839 16047-16112, 10.5194/acp-13-9869-2013, 2013a.
840 Zhao, M., Zhang, Y., Ma, W., Fu, Q., Yang, X., Li, C., Zhou, B., Yu, Q., and Chen, L.: Characteristics
841 and ship traffic source identification of air pollutants in China's largest port, Atmos. Environ., 64, 277-
842 286, 2013b.
843 Zhao, P. S., Dong, F., He, D., Zhao, X. J., Zhang, X. L., Zhang, W. Z., Yao, Q., and Liu, H. Y.:
844 Characteristics of concentrations and chemical compositions for PM2.5 in the region of Beijing, Tianjin,
845 and Hebei, China, Atmos. Chem. Phys., 13, 4631-4644, 10.5194/acp-13-4631-2013, 2013c.
846 Zhao, R., Han, B., Lu, B., Zhang, N., Zhu, L., and Bai, Z.: Element composition and source
847 apportionment of atmospheric aerosols over the China Sea, Atmos. Pollut. Res., 6, 191-201, 2015.
848 Zhao, X. J., Zhao, P. S., Xu, J., Meng, W., Pu, W. W., Dong, F., He, D., and Shi, Q. F.: Analysis of a
849 winter regional haze event and its formation mechanism in the North China Plain, Atmos. Chem. Phys.,
850 13, 5685-5696, 10.5194/acp-13-5685-2013, 2013d.
851 Zhou, D., Li, B., Huang, X., Virkkula, A., Wu, H., Zhao, Q., Qiao, Y., Shen, G., Ding, A., Zhang, J., Liu,

852 Q., Li, L., Li, C., Chen, F., and Yuan, S.: The Impacts of Emission Control and Regional Transport on
853 PM2.5 Ions and Carbon Components in Nanjing during the 2014 Nanjing Youth Olympic Games,
854 Aerosol. Air. Qual. Res., 17, 730-740, 10.4209/aaqr.2016.03.0131, 2017.
855 Zhou, M., Qiao, L., Zhu, S., Li, L., Lou, S., Wang, H., Wang, Q., Tao, S., Huang, C., and Chen, C.:
856 Chemical characteristics of fine particles and their impact on visibility impairment in Shanghai based on
857 a 1-year period observation, J. Environ. Sci. (China), 48, 151-160, 2016.
858 Zou, Y., Deng, X. J., Zhu, D., Gong, D. C., Wang, H., Li, F., Tan, H. B., Deng, T., Mai, B. R., and Liu,
859 X. T.: Characteristics of 1 year of observational data of VOCs, NOx and O3 at a suburban site in
860 Guangzhou, China, Atmos. Chem. Phys., 15, 6625-6636, 10.5194/acp-15-6625-2015, 2015.

861

Captions of Figure and Table

Table 1. The detailed information of $PM_{2.5}$ and $PM_{1.0}$ in the ambient during YRC.

Table 2. The pollutant levels and meteorological parameters in eight different episodes.

Table 3. The average concentration of the elements in $PM_{2.5}$ and $PM_{1.0}$ (ng m^{-3}) during YRC

Table 4. Comparisons of trace element concentrations with the reported data (μg m^{-3}).

Figure 1. Cruise tracks, source region limits, the sampling sites, and land use during YRC.

Figure 2. The average distribution of (a) aerosol optical depth at 550nm (MODIS L2); (b) CO column mixture ratio (MOPITT L2); (c) the SO_2 column concentration (OMI L2); (d) the NO_2 column concentration (OMI L2) over MLYR region.

Figure 3. Spatial concentration distributions of the soluble ions and levoglucosan in $PM_{2.5}$ along the cruise path.

Figure 4. Comparisons major ionic species during YRC with other regions, including: Beijing, Xi'an, Chengdu, Wuhan, Guangzhou, Shanghai, Northern South China Sea, Taiwan Strait, South China Sea, East China Sea and Tuoji Island. The red lines mark the sample routes in different cruises.

Figure 5. (a) Principal component analysis (PCA) of the typical elements in $PM_{2.5}$; **(b)** Time series of four typical element sources derived from PCA. All of the units are in μg m^{-3}.

Figure 6. Probable sources from PSCF for individual elements in $PM_{2.5}$ during YRC. The criteria are the mean concentration for all.

Figure 7. Time serious of V concentration (read column), estimates of primary $PM_{2.5}$ from ship emission, and number of ship distribution in the Yangtze River channel during YRC.

Table 1

Sample Number	Start data UTC	Day/Night Samples	Ship state	Sampling duration	Average Latitude, °N	Average Longitude, °E	$PM_{2.5}$ (μg m^{-3})	$PM_{1.0}$ (μg m^{-3})	$PM_{1.0}/PM_{2.5}$
#1	25-Nov-15	Daily	Moving	24 hours	30.95	117.78	63.83	58.30	91.33%
#2	26-Nov-15	Daily	Moving	24 hours	30.30	116.95	112.70	84.58	75.06%
#3	27-Nov-15	Daily	Moving	24 hours	29.73	115.86	106.40	90.37	84.96%
#4	28-Nov-15	Daily	Moving	24 hours	30.37	115.06	81.49	73.69	90.43%
#5	29-Nov-15	Daytime	Moving	12 hours	30.63	114.53	157.70	136.10	86.32%
#6	29-Nov-15	Nighttime	Stopping	12 hours	30.69	114.45	161.80	152.20	94.06%
#7	30-Nov-15	Daytime	Moving	12 hours	30.42	114.92	80.56	65.56	81.38%
#8	30-Nov-15	Nighttime	Stopping	12 hours	30.09	115.32	106.30	89.29	83.99%
#9	1-Dec-15	Daytime	Moving	12 hours	29.72	115.97	96.00	81.83	85.24%
#10	1-Dec-15	Nighttime	Moving	12 hours	30.32	116.89	92.02	82.86	90.04%
#11	2-Dec-15	Daytime	Moving	12 hours	31.08	117.96	122.80	85.17	69.34%
#12	2-Dec-15	Nighttime	Moving	12 hours	31.90	118.55	163.20	118.40	72.55%
#13	3-Dec-15	Daytime	Moving	12 hours	32.27	119.44	152.90	108.70	71.09%
#14	3-Dec-15	Nighttime	Moving	12 hours	31.95	120.27	133.90	105.60	78.89%
#15	4-Dec-15	Daytime	Moving	12 hours	31.70	121.18	146.10	111.80	76.57%
#16	4-Dec-15	Nighttime	Stopping	12 hours	31.38	121.60	131.20	102.70	78.27%

Table 2

Periods	Data and time (BST[a])	Latitude	Longitude	wind speed (m/s)	RH%	NOx (ppb)	SO_2 (ppb)	CO (ppb)	$PM_{2.5}$ (SN[b])	T/B
EP-1	2015/11/22 12:00 to 2015/11/23 18:00	31.28 to 32.22	121.23 to 119.55	3.01	88.95	65.51	6.32	443.91		1.59
EP-2	2015/11/25 12:00 to 2015/11/27 14:00	31.01 to 29.91	117.79 to 116.35	2.86	66.73	57.50	12.45	704.48	(#1,2)	0.81
EP-3	2015/11/27 14:00 to 2015/11/29 00:00	29.84 to 30.50	116.35 to 114.83	2.48	69.72	68.16	16.15	676.20	(#3,4)	1.49
EP-4	2015/11/29 00:00 to 2015/11/30 18:00	30.50 to 30.18	114.83 to 115.25	2.18	83.01	62.65	8.60	1030.25	(#5-7)	0.97
EP-5	2015/11/30 18:00 to 2015/12/01 20:00	30.18 to 30.02	115.25 to 116.66	2.32	79.64	51.92	11.66	989.75	(#8,9)	2.61
EP-6	2015/12/01 20:00 to 2015/12/02 20:00	30.02 to 31.67	116.66 to 118.40	3.84	74.67	31.00	4.09	1139.33	(10,11)	0.96
EP-7	2015/12/02 20:00 to 2015/12/03 20:00	31.67 to 32.32	118.40 to 119.73	5.39	44.91	23.73	7.87	1224.88	(#12,13)	1.00
EP-8	2015/12/03 20:00 to 2015/12/05 06:00	32.32 to 31.36	119.73 to 121.61	2.68	38.86	57.55	16.62	1061.46	(#14-16)	1.73

[a] Beijing standard time (GMT-8); T/B is ratio of toluene to benzene; [b] sample number in Table 1.

Table 3

Contents		Average	Max	Min	Median	SD[a]
Mg	$PM_{2.5}$	629.87	1487.67	135.69	589.13	358.57
	$PM_{1.0}$	328.57	699.09	17.26	359.42	213.44
Al	$PM_{2.5}$	863.87	2400.13	21.13	786.17	618.66
	$PM_{1.0}$	631.37	1894.40	100.78	473.46	483.74
K	$PM_{2.5}$	865.88	1723.87	368.51	805.73	367.14
	$PM_{1.0}$	771.80	1560.67	326.41	739.86	303.33
Ca	$PM_{2.5}$	2724.35	5657.60	391.54	2381.94	1729.51
	$PM_{1.0}$	1525.39	3371.73	108.21	1455.19	1108.03
V	$PM_{2.5}$	9.71	60.00	0.19	7.33	13.45
	$PM_{1.0}$	9.20	55.50	1.18	6.80	12.72
Cr	$PM_{2.5}$	22.29	62.67	2.16	16.73	16.51
	$PM_{1.0}$	21.67	48.17	2.67	22.74	13.31
Mn	$PM_{2.5}$	56.63	152.12	9.08	42.56	43.42
	$PM_{1.0}$	45.80	106.33	8.58	31.56	31.75
Fe	$PM_{2.5}$	1644.84	5188.18	38.87	860.40	1590.29
	$PM_{1.0}$	934.30	2616.83	46.74	516.37	850.12
Co	$PM_{2.5}$	0.82	2.88	0.00	0.48	0.75
	$PM_{1.0}$	0.62	1.67	0.07	0.26	0.53
Ni	$PM_{2.5}$	10.53	73.64	1.83	5.61	16.82
	$PM_{1.0}$	8.19	32.29	1.39	4.35	7.89
Cu	$PM_{2.5}$	18.79	49.87	4.07	17.66	11.28
	$PM_{1.0}$	15.21	37.07	3.70	12.32	7.87
Zn	$PM_{2.5}$	295.08	638.08	125.36	221.83	159.05
	$PM_{1.0}$	288.84	485.26	81.91	261.06	156.34
As	$PM_{2.5}$	37.33	107.17	0.87	31.50	28.14
	$PM_{1.0}$	41.73	111.85	12.46	30.70	32.00
Se	$PM_{2.5}$	6.08	12.18	2.70	5.78	2.57
	$PM_{1.0}$	6.48	11.04	3.07	6.40	2.76
Cd	$PM_{2.5}$	2.72	5.00	1.30	2.50	1.06
	$PM_{1.0}$	5.42	39.20	1.30	3.33	9.09
Tl	$PM_{2.5}$	0.32	0.90	0.00	0.29	0.22
	$PM_{1.0}$	0.41	0.89	0.14	0.35	0.23
Pb	$PM_{2.5}$	98.37	176.54	53.26	95.68	35.91
	$PM_{1.0}$	110.45	274.80	53.04	102.84	54.07

[a] SD is one standard deviation.

Table 4

	2015[a]	2003	2011	2013-2014	2012-2013	2011	2012-2013	2008-2009	2009-2010
	(this study)	(Zhang et al., 2007)	(Zhao et al., 2015)	(Li et al., 2016)	(Lai et al., 2016)	(Tao et al., 2014)	(Zhang et al., 2015)	(Huang et al., 2013)	(Zhao et al., 2013)
	Winter	Spring	Spring	Winter	Winter	Winter	Winter	Winter	Winter
	Yangtze River channel[b]	Northern South China Sea	East China sea	Taiwan strait	Guangzhou (rural)	Chengdu	Wuhan	Shanghai	Beijing
Al	0.86	0.31	3.28	3.00	0.21	0.43	—	0.64	1.03
Ca	2.72	0.82	2.40	2.00	0.11	0.26	2.27	0.72	1.85
Fe	1.64	0.32	1.37	1.30	0.16	0.61	1.42	0.56	1.55
Mg	0.63	0.11	0.83	2.40	2.30	0.16	0.61	0.26	0.57
As	0.04	—	0.01	—	—	0.02	0.04	0.02	0.01
Cd	0.00	—	—	—	—	0.00	0.01	—	—
Cr	0.02	0.03	—	0.60	—	0.01	0.01	0.02	0.01
Cu	0.02	—	0.01	—	0.03	0.03	0.03	0.04	0.04
Mn	0.06	—	0.01	0.70	0.03	0.07	0.13	0.04	0.09
Ni	0.01	—	0.01	0.90	—	0.00	0.01	0.01	0.01
Pb	0.10	0.16	0.02	0.70	0.09	0.20	0.24	0.06	0.15
V	0.01	—	0.02	—	—	0.00	—	0.01	—
Zn	0.30	—	0.07	0.60	0.27	0.32	0.37	0.13	0.30

[a] Sampling periods; [b] Sampling sites

Figure 1.

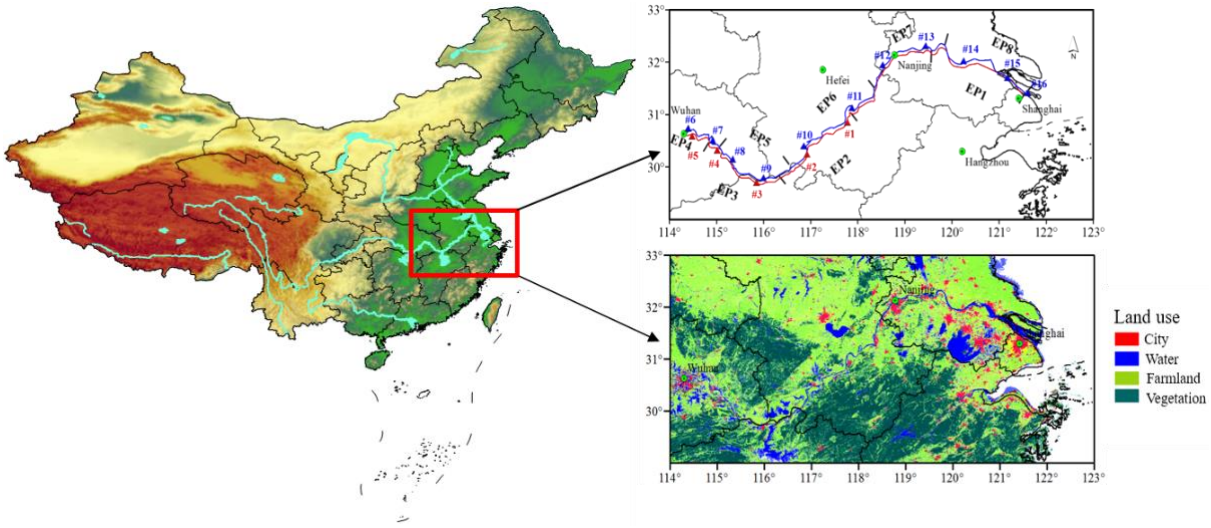
Hefei
Nanjing
Wuhan
Shanghai
Hangzhou
EP1
EP2
EP3
EP4
EP5
EP6
EP7
EP8
#1
#2
#3
#4
#5
#6
#7
#8
#9
#10
#11
#12
#13
#14
#15
#16
114°
115°
116°
117°
118°
119°
120°
121°
122°
123°
33°
32°
31°
30°
Land use
City
Water
Farmland
Vegetation

Figure 2.

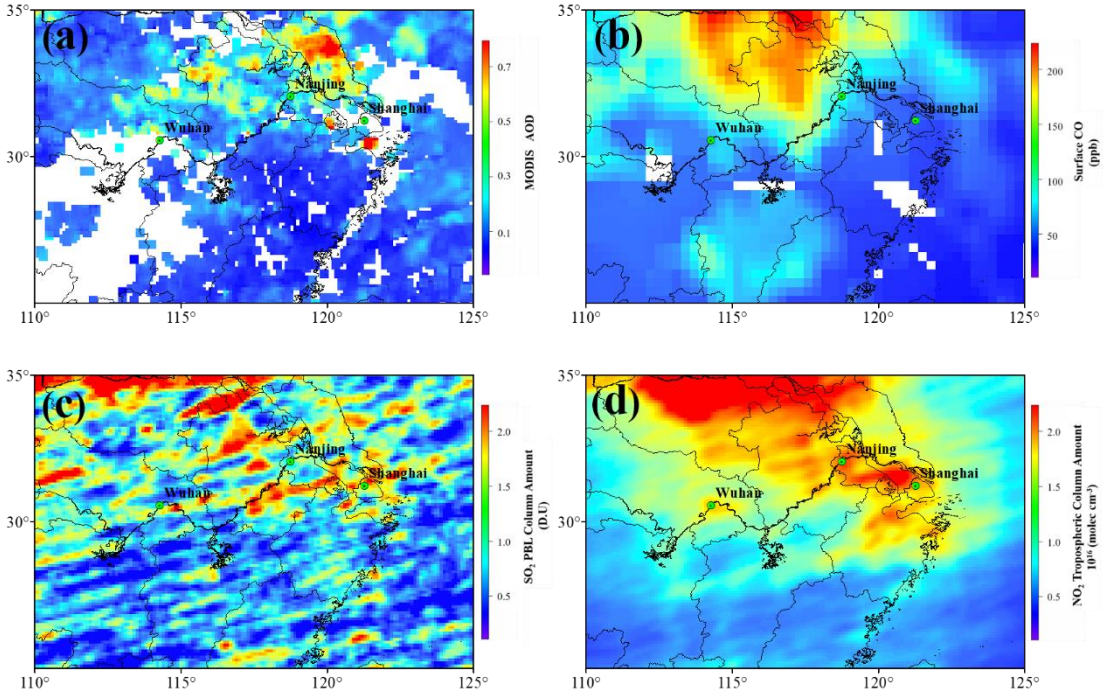
(a)
(b)
(c)
(d)
Nanjing
Shanghai
Wuhan
35°
30°
110°
115°
120°
125°
MODIS AOD
Surface CO (ppb)
SO2 PBL Column Amount (D.U)
NO2 Tropospheric Column Amount 10^15 (molec cm^-2)

Figure 3.

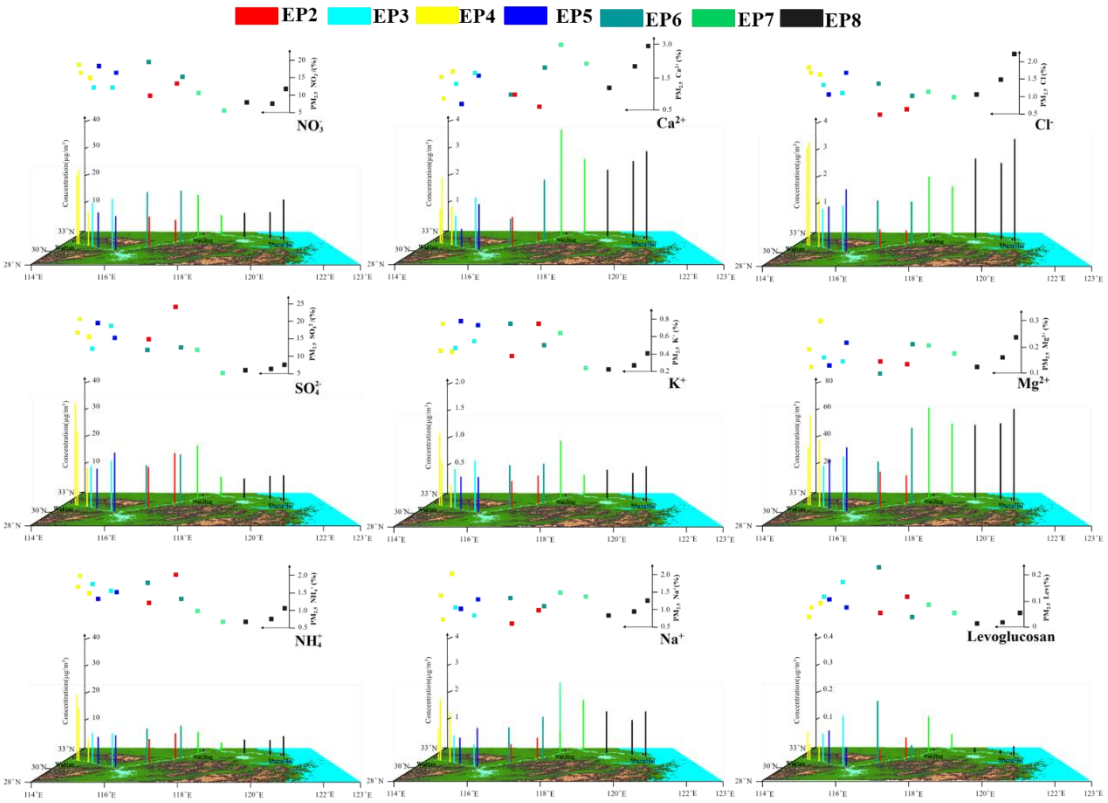
EP2
EP3
EP4
EP5
EP6
EP7
EP8
NO3-
Ca2+
Cl-
SO42-
K+
Mg2+
NH4+
Na+
Levoglucosan

Figure 4.

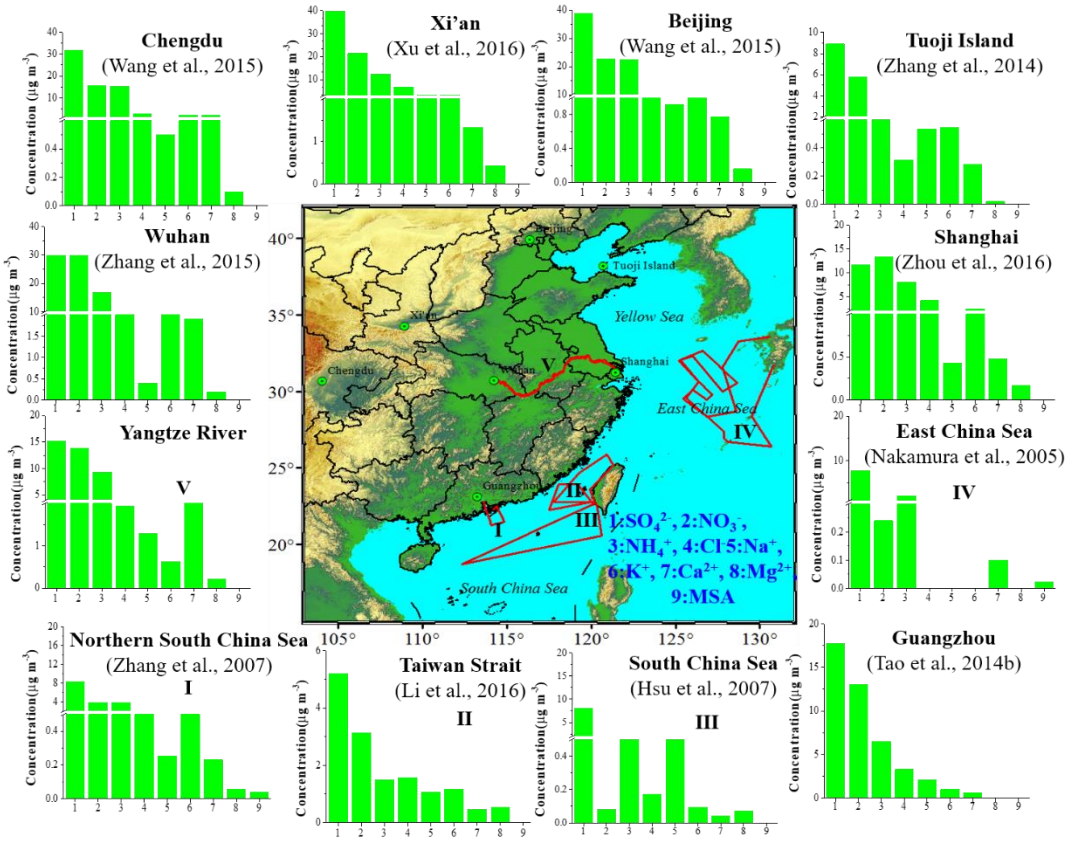
Chengdu
(Wang et al., 2015)
Xi'an
(Xu et al., 2016)
Beijing
(Wang et al., 2015)
Tuoji Island
(Zhang et al., 2014)
Wuhan
(Zhang et al., 2015)
Shanghai
(Zhou et al., 2016)
Yangtze River
V
East China Sea
(Nakamura et al., 2005)
IV
Northern South China Sea
(Zhang et al., 2007)
I
Taiwan Strait
(Li et al., 2016)
II
South China Sea
(Hsu et al., 2007)
III
Guangzhou
(Tao et al., 2014b)
Concentration (μg m-3)
Yellow Sea
East China Sea
South China Sea
Beijing
Tuoji Island
Xi'an
Shanghai
Chengdu
Wuhan
Guangzhou
1:SO4 2-, 2:NO3-,
3:NH4+, 4:Cl-5:Na+,
6:K+, 7:Ca2+, 8:Mg2+,
9:MSA
105°
110°
115°
120°
125°
130°
40°
35°
30°
25°
20°

Figure 5.

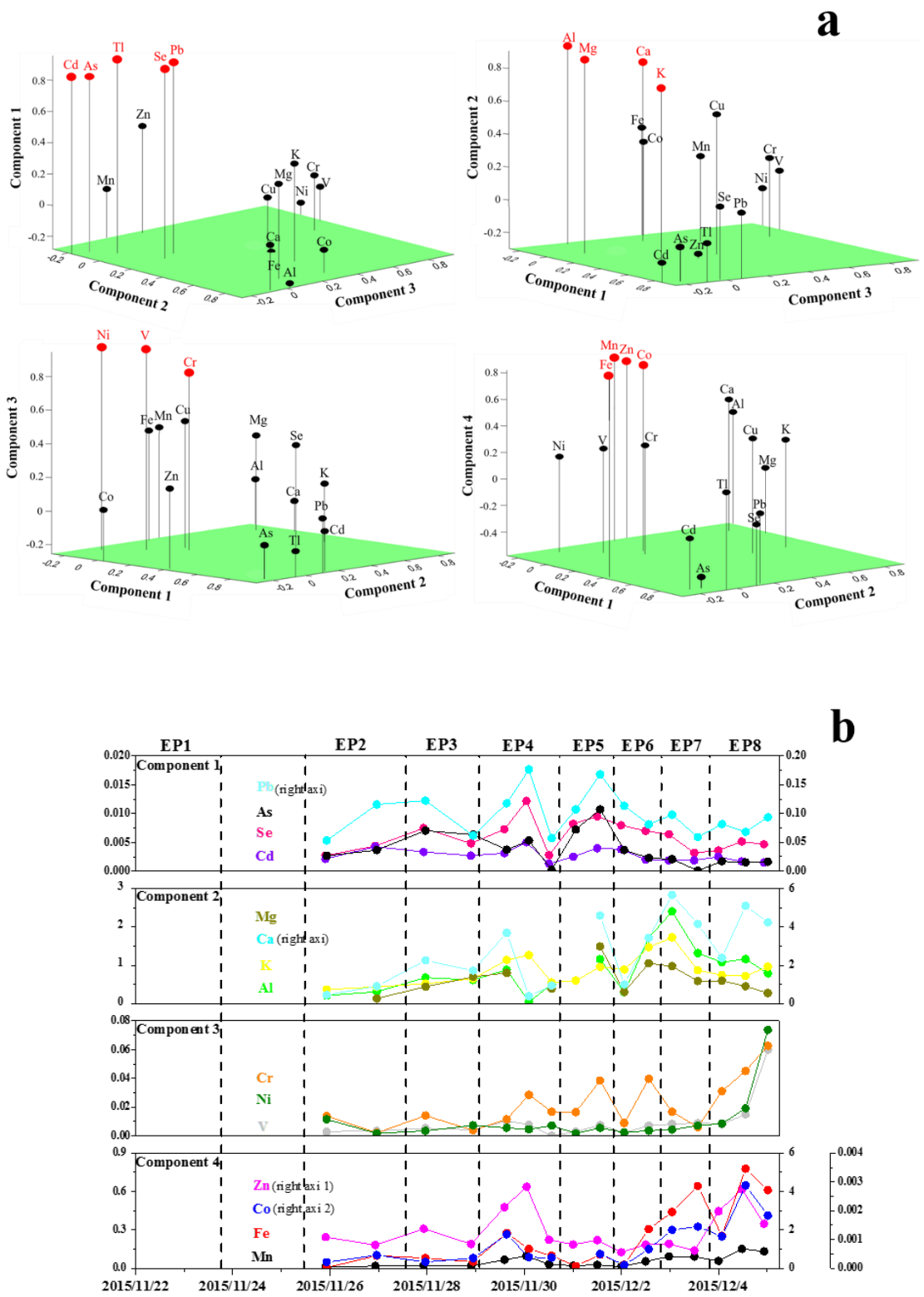
a
Component 1
Component 2
Component 3
Component 4
b
EP1
EP2
EP3
EP4
EP5
EP6
EP7
EP8
Component 1
Pb (right axi)
As
Se
Cd
Component 2
Mg
Ca (right axi)
K
Al
Component 3
Cr
Ni
V
Component 4
Zn (right axi 1)
Co (right axi 2)
Fe
Mn
2015/11/22
2015/11/24
2015/11/26
2015/11/28
2015/11/30
2015/12/2
2015/12/4

Figure 6.

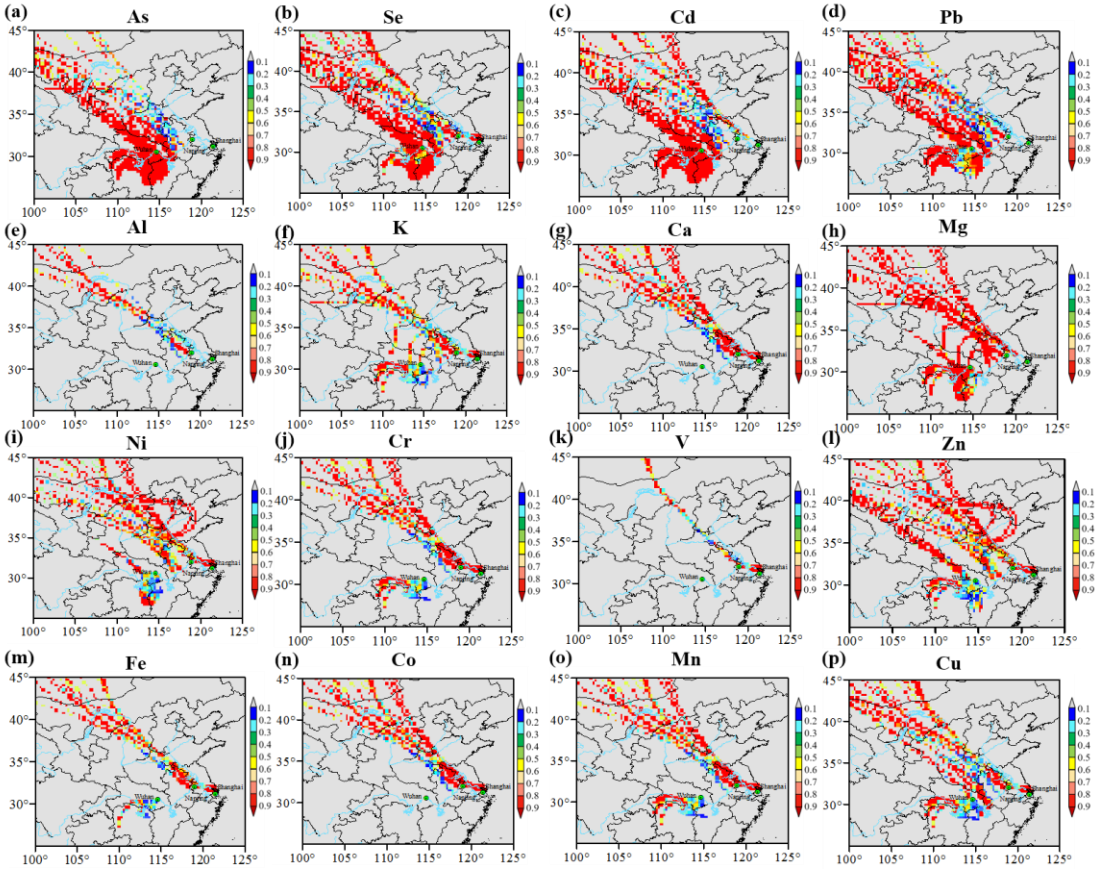

Figure 7.

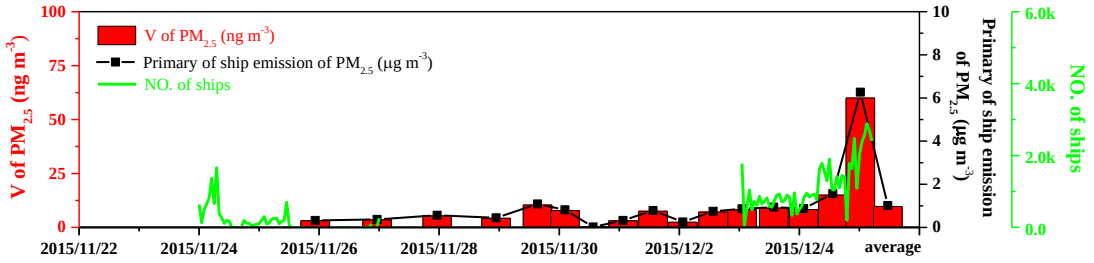
V of PM2.5 (ng m-3)
Primary of ship emission of PM2.5 (μg m-3)
NO. of ships
V of PM2.5 (ng m-3)
Primary of ship emission of PM2.5 (μg m-3)
NO. of ships
100
75
50
25
0
10
8
6
4
2
0
6.0k
4.0k
2.0k
0.0
2015/11/22
2015/11/24
2015/11/26
2015/11/28
2015/11/30
2015/12/2
2015/12/4
average